Julian Piatek

Characterisation of $LiHo_xEr_{1-x}F_4$ alloyed Model Magnets

Professor: Hernik Rønnow
Supervisor: Ivica Zivkovic

École Polytechnique Fédérale de Lausanne (EPFL)
Laboratory for Quantum Magnetism (LQM)

January 12, 2009

Contents

List of Figures

1 Introduction

In the field which can be broadly described as experimental quantum magnetism, there are in general two kind of systems. Systems showing some interesting behaviour for which the Hamiltonian is unknown and must be characterised are the first possible system. The second type of system, which will be discussed in this thesis is a system where the Hamiltonian is well known and thus the theoretical models used can be tested. The system in question is $LiHo_xEr_{1-x}F_4$; a system which goes from an Ising ferromagnet when x=1 to an x-y planar antiferromagnet when x=0. It is expected that somewhere in between these two concentrations the system will become a re-entrant spin glass due to the combination of disorder and frustration caused by replacing Ho^{3+} with Er^{3+}.

1.1 Spin Glasses

Before delving into the topic of spin glasses, the idea of short range order must be introduced. The term short range order is often used to describe systems which have correlations that fluctuate in space and time, and whose correlation length grows with decreasing temperature. These correlations may diverge at a long range ordering transition, at which point the relaxation time will also diverge. The relaxation rate in such a system is in the GHz range. Another meaning of the term short range order is once again that there are correlations, however in this case the correlations are frozen, or almost frozen in space and time. The idea of the correlation being in a frozen state, implies that the relaxation time is macroscopically long, with a relaxation rate in the mHz to kHz range. It should be noted that in this text, when the term short range order is used, it implicitly implies a frozen / near frozen short range order.

A spin glass is a magnetic state which is distinct from the long range ordered states of ferromagnetic and antiferromagnetic phases. While being distinct from these states, many of the properties found in the long range ordered states are also present in spin glasses, such as the collective nature in the frozen state. A spin glass requires several ingredients to be formed, which include disorder and frustration.

Disorder, or randomness, required to form a spin glass can come from several sources. The most simple disorder found is a random site disorder - only some of the sites in the crystalline structure are magnetic and they are placed randomly in the crystal. The

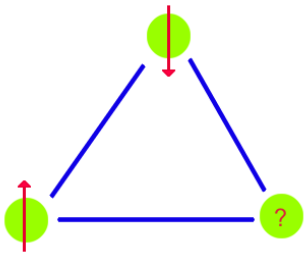

Figure 1.1: A simple example of frustration. If the three spins have anti-parallel interactions, it is not possible to satisfy all three interactions at once.

archetypal examples of random site disorder spin glasses are $Cu_{1-x}Mn_x$ and $Au_{1-x}Fe_x$, where magnetic ions are placed randomly into an inert metallic matrix. These spin glasses are known as canonical spin glasses. A second method of creating disorder in a crystal is to simply destroy the crystalline structure and make the system amorphous. The final way of obtaining random spins through site disorder is site substitution. In this process, a crystal is grown which can either have a magnetic or non-magnetic ion in a certain position in the crystal structure. By using a solute containing both magnetic and non-magnetic ions in the correct proportions, the spins are placed randomly throughout the compound. In addition to this site disorder, bond-disorder can also be used to create a system of random spins. In this case the crystal lattice remains perfect, but the spins themselves will have a different interaction depending on whether the coupling is parallel or anti-parallel.

A spin glass is governed by the interactions between the spins as these will give the overall cooperative behaviour and indeed the very formation of the spin glass. For a spin glass to form there must be some kind of frustration. The most simple example of frustration is that of a triangle of spins which have an antiferromagnetic coupling as is illustrated in Figure 1.1. If the left spin is pointing up and the spin at the top of the triangle is pointing down, then there is no way for the spin on the right to satisfy both bonds antiferromagnetically. When this phenomena is encountered for large number of the spins in the system, the system is frustrated. The frustration creates a multidegenerate, metastable and frozen ground state for the spin glass system.

The key element to creating a spin glass is to have both frustration and disorder. If a system were to be completely frustrated, such as the triangular spin system already mentioned, a spin glass state would not be formed. It also seems that having just antiferromagnetic interactions and disorder is not enough to create a spin glass [18]. The key here is to have spins which are disordered and frustrated with a combination of ferro and antiferromagnetic interactions. When this is achieved, the system, when cooled below T_f will freeze into the spin glass state.

To briefly describe in a very qualitative way the freezing process, imagine a spin glass

system at T $\rightarrow \infty$. It is clear that at this temperature a paramagnetic behaviour will be observed due to the high temperature. As the temperature is lowered, but still keeping T $\gg$ T$_f$, some spins will begin to cluster or even form domains. There will remain some spins which are not inside these clusters that will help to mediate interactions between different clusters. Decreasing the temperature further will begin to remove the disorder, allowing for longer-range interactions, and as T $\rightarrow$ T$_f$, various spin components will begin to interact with each other. The spins will align themselves to seek out ground state (T= 0), however due to the degeneracy introduced by the frustration, the system may become trapped in a metastable configuration of higher energy [18].

In this frozen state T $\ll$ T$_f$, many strange magnetic phenomena are observed. Most of these phenomena are related to the application of large DC fields. In the glassy state, there is quite often a 'memory', that is to say a system which is cooled and then a magnetic field is applied could behave differently to one which is cooled with the magnetic field already applied [5]. Another interesting effect observed in spin glasses is the ability to perform spectral hole burning using RF frequencies [9].

1.2 The Li*ReF*$_4$ System

The lithium rate earth fluorides have on the whole been studied for quite some time. The earliest studies determined that some of these insulators showed magnetic order at low temperature and calculated the crystal field parameters for several members of the Li*Re*F$_4$ (where *Re* represents rare earth) family [3, 4, 10, 15, 16, 17]. The Li*Re*F$_4$ family was found to order either ferromagnetically with Ising spins or planar antiferromagnetically, thus the only apparent interest in these systems was as realisations of some of the simplest magnetic systems. These systems were mainly studied as simple model magnets until the realisation that by doping LiHoF$_4$ with large enough concentrations of yttrium, a spin glass can form [24].

The crystal structure of the Li*Re*F$_4$ system is crystallographically very well characterised. It is has a body-centered tetragonal structure with the rare earth (Re^{3+}) ions at the sites $\vec{r_1} = (0, 0, \frac{1}{2}c)$, $\vec{r_2} = (\frac{1}{2}a, 0, \frac{3}{4}c)$, $\vec{r_3} = (\frac{1}{2}a, \frac{1}{2}a, c)$, $\vec{r_4} = (\frac{1}{2}a, 0, \frac{1}{4}a)$. The unit cell of this structure is shown in Figure 1.2. The unit cell parameters for the entire family have been determined, and those relevant to the work carried out are shown in Table 1.1. It is important to note that although there are four different sites for the Re^{3+} ions, they are all magnetically equivalent.

Low temperature investigations of various Li*Re*F$_4$ have shown that the long range dipole dipole interactions dominate the magnetic couplings. It should however be noted that the superexchange interactions have been found to be non-negligible at very low temperatures [3, 17]. As will be discussed later, the type of ordered states formed depends essentially

Compound	c [Å]	a [Å]	c / a	Unit Cell Volume [Å^3]
$LiHoF_4$	10.75	5.175	2.077	287.9
$LiErF_4$	10.70	5.162	2.073	285.1
$LiYF_4$	10.74	5.175	2.075	287.6

Table 1.1: Unit Cell Parameters for $LiHoF_4$, $LiErF_4$ and $LiYF_4$ (taken from [17])

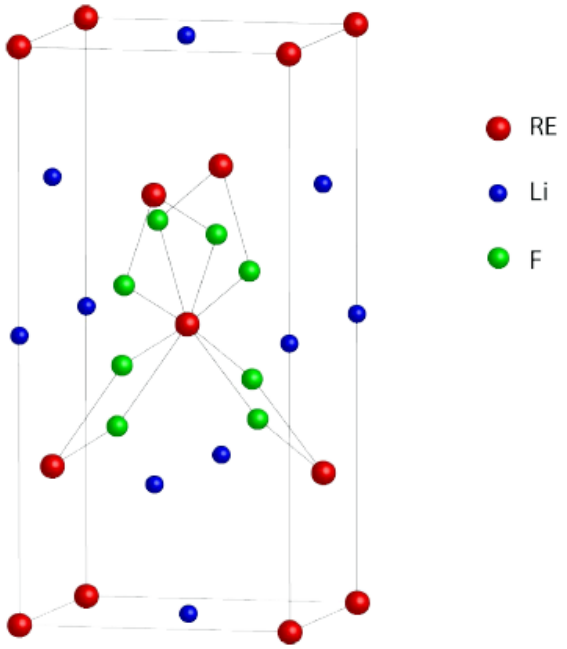

Figure 1.2: Diagram showing the body-centered tetragonal crystal structure of the LiReF$_4$ system.

only on the crystal field parameters and the dipole-dipole interaction.

1.2.1 Lithium Holmium Fluoride

$LiHoF_4$ was first studied as a model Ising ferromagnet. It was found to order at a temperature of 1.30 K [10], which was later refined to 1.53K. The domain size is on the order of 5 μm and the spins point preferentially along the crystallographic c axis [2]. Theoretical calculations give the energy of the ground state in terms of the splitting factors $g_\parallel$ and $g_\perp$, finding that if $g_\parallel/g_\perp > 1.01$ ferromagnetic order is expected [17]. Various measurement methods have shown that $g_\parallel = 13.3 - 13.8$ [16] and $g_\perp \approx 0.74$ [6], thus the ferromagnetic order seen is in agreement with the theory. Due to the long range of the dipole-dipole coupling, which give rise to the ordered state, the mean field critical dimensionality is reduced from four to three [1], meaning that $LiHoF_4$ is a mean field magnet.

Recent work on $LiHoF_4$ has mainly focused on adding disorder to the Ising system and also investigating quantum phase transitions. Disorder has been added by replacing a fraction of the Ho^{3+} ions with Y^{3+} ones. As the Y^{3+} ions have no effective spin, they add disorder to the system without perturbing the Ho spins too much. As for the quantum phase transitions, it was found that applying a large DC field perpendicular to the Ising axis causes the system to go through a quantum phase transition [6] and this transition has been studied in great detail [26]. Various concentrations of $LiHo_xY_{1-x}F_4$ have been studied in depth using AC susceptibility, specific heat and neutron scattering to name a few methods. Properties such as the quantum fluctuations [7], non-linear effects [9] and relaxation [29] of the resulting spin glass were studied. Even though so much research has gone into these compounds, it is still debated whether a spin glass state actually forms, although the latest calculations seem to agree with experiments that spin glasses do indeed form [23, 22, 28].

1.2.2 Lithium Erbium Fluoride

$LiErF_4$ is an x-y planar antiferromagnet, with the spins lying on in the a-b plane of the tetragonal crystal. It is interesting to note that for some time, theoretical calculations predicted $LiErF_4$ would order ferromagnetically [10]. AC susceptbility measurements finally showed that the order is in fact antiferromagnetic in nature, with $T_N = 0.381 \pm 0.005$ K [3]. There are three possible antiferromagnetic configurations for $LiErF_4$ [17], which are represented in Figure 1.3. A layered antiferromagnetic order (LAFM), either along the x or y direction, could form, or the system could order as a pure antiferromagnet (AFM). Specific heat measurements determined that $LiErF_4$ would order into one of the two LAFM states [16], with each being energetically equivalent.

$LiErF_4$ has not had as much interest as $LiHoF_4$ as it would not seem to be too interesting

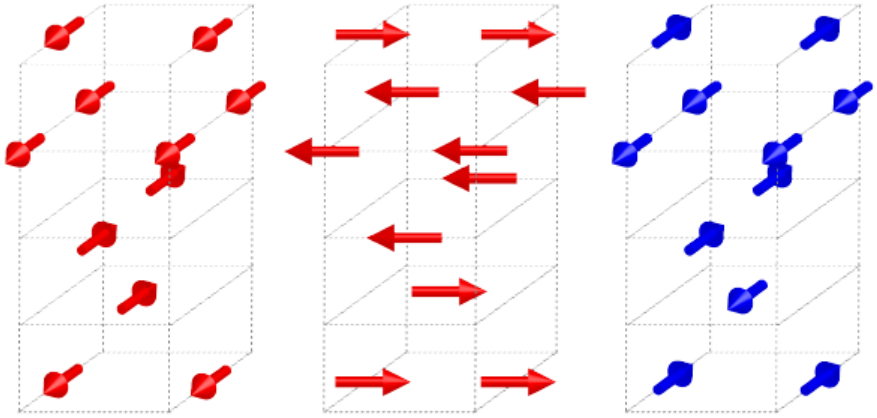

Figure 1.3: Planar antiferromagnetic structure of $LiErF_4$. The two sets of images on the left illustrate the layered antiferromagnetic order and the image with blue arrows that of a pure antiferromagnet. (Image taken from [14])

to attempt to add disorder to this kind of system. As was the case with $LiHoF_4$, the initial work carried out on this system was a determination of crystal parameters and ordering temperature [3, 4, 10]. More recent work has focused on the possibility of a quantum phase transition in $LiErF_4$ using specific heat and neutron scattering measurements [14, 13].

In this work presented here, the inter $LiErF_4$ is that using Er instead of Y as a dopant could be very interesting. There have already been many interesting results published on $LiHo_xY_{1-x}F_4$, most of which are related to the glassy behaviour encountered. As the formation of a glass requires both disorder and frustration, changing the dopant ion from a non-magnetic one to one which has a very large spin ($J = {}^{15}/_{2}$) has the potential to enhance the onset of any glass-like properties.

2 Theory

This section briefly describes the Hamiltonian of the LiReF$_4$ system showing the main interactions which give this system its properties. After the system has been detailed, the mean field calculation will be introduced and subsequently applied to LiHo$_x$Er$_{1-x}$F$_4$ using the virtual crystal approximation.

2.1 The Li*Re*F$_4$ system

The LiReF$_4$ has a well characterised Hamiltonian, which combines the crystal field, hyperfine and Zeeman interactions, the classical dipole tensor and a nearest neighbour term.

$$\mathcal{H} = \sum_i [\mathcal{H}_{CF}(\mathbf{J}_i) + A\mathbf{J}_i \cdot \mathbf{I}_i - g\mu_B \mathbf{J}_i \cdot H] - \frac{1}{2}\sum_{ij}\sum_{\alpha\beta} \mathcal{J}_D D_{\alpha\beta}(ij)\mathbf{J}_{i\alpha}\mathbf{J}_{i\beta} - \frac{1}{2}\sum_{ij}^{n.n} \mathcal{J}_{12}\mathbf{J}_i \cdot \mathbf{J}_j \quad (2.1)$$

where $\mathcal{H}_{\mathcal{CF}}$ is the crystal field Hamiltonian, which is given by

$$\mathcal{H}_{\mathcal{CF}} = \sum_{l=2,4,6} B_l^0 \mathbf{O}_l^0 + \sum_{l=4,6} B_l^4(c)\mathbf{O}_l^4(c) + B_6^4(s)\mathbf{O}_6^4(s) \quad (2.2)$$

and $D_{\alpha\beta}(ij)$ is the classical dipole tensor , which takes the standard form

$$D_{\alpha\beta}(ij) = \frac{3(r_{i\alpha} - r_{j\alpha})(r_{i\beta} - r_{j\beta}) - |\mathbf{r}_i - \mathbf{r}_j|^2\delta_{\alpha\beta}}{|\mathbf{r}_i - \mathbf{r}_j|^5} \quad (2.3)$$

the Hyperfine interaction is given by

$$\sum_i A\mathbf{J}_i \cdot \mathbf{I}_i \quad (2.4)$$

and the Zeeman term by

$$-\sum_i g\mu_B \mathbf{J}_i \cdot H \quad (2.5)$$

finally the nearest neighbour term is

$$-\frac{1}{2}\sum_{ij}^{n.n}\mathcal{J}_{12}\mathbf{J}_i\cdot\mathbf{J}_j \tag{2.6}$$

In (2.1), $\mathbf{J}_i$ and $\mathbf{I}_i$ are, respectively, the electronic angular momentum and the nuclear spin of the ith ion. For Er $\mathbf{I}=6$ and $\mathbf{J}=15/2$, and for Ho $\mathbf{I}=6$ and $\mathbf{J}=8$.

Two terms which dominate the magnetic properties of the system are the crystal field parameters and the dipole-dipole interactions. The former by is given by both the crystal field parameters, B_m^n, and the Stevensoperators, $\mathbf{O}_m^n$, which are given following the convention described by Hutchings [11]:

$$\begin{aligned}
\mathbf{O}_2^0 &= 3\mathbf{J}_z^2 - X \\
\mathbf{O}_4^0 &= 35\mathbf{J}_z^4 - (30X-25)\mathbf{J}_z^2 + 3X^2 - 6X \\
\mathbf{O}_4^4 &= \frac{1}{2}(\mathbf{J}_+^4 - \mathbf{J}_-^4) \\
\mathbf{O}_6^0 &= 231\mathbf{J}_z^6 - (315X-735)\mathbf{J}_z^4 + (105X^2-525X+294)\mathbf{J}_z^2 \\
&\qquad -5X^3+40X^2-60X \\
\mathbf{O}_6^4(c) &= \frac{1}{4}[(11\mathbf{J}_z^2 - X - 38)(\mathbf{J}_+^4+\mathbf{J}_-^4) + (\mathbf{J}_+^4+\mathbf{J}_-^4)(11\mathbf{J}_z^2 - X - 38)] \\
\mathbf{O}_6^4(s) &= \frac{1}{4i}[(11\mathbf{J}_z^2 - X - 38)(\mathbf{J}_+^4-\mathbf{J}_-^4) + (\mathbf{J}_+^4-\mathbf{J}_-^4)(11\mathbf{J}_z^2 - X - 38)]
\end{aligned} \tag{2.7}$$

The crystal field parameters have been measured for both $LiHoF_4$ and $LiErF_4$ and are given below.

Compound	B_2^0	$10^3B_4^0$	$10^3B_4^4$	$10^5B_6^0$	$10^5B_6^4(c)$	$10^5B_6^4(s)$
$LiErF_4$	0.059	-0.18	-4.36	-0.180	-8.79	-2.77
$LiHoF_4$	-0.06	0.35	3.6	0.04	7.0	$\pm$0.98

Table 2.1: Crystal field parameters for $LiHoF_4$ (taken from [26]) and $LiErF_4$ (taken from [14])

2.2 Possible Theoretical Methods

To determine the magnetic behaviour of a microscopic system on a macroscopic level, it is normally not possible to get an exact solution. The reason is that there are simply too many variables and the problem becomes extremely complex at an alarming rate. There are essentially two ways in which the problem can be solved. The first is by using a Monte-Carlo method to simulate the system, which will in general follow the following pattern:

1. Define a domain of possible inputs.

2. Generate inputs randomly from the domain.

3. Perform a deterministic computation using the inputs.

4. Aggregate the results of the individual computations into the final result.

This kind of computation is unfortunately still rather limited as the size of the spin system must be relatively small to be able to do the calculations.

The other method which is generally used is a mean field approximation. In this computation, a single interaction is calculated and the resulting value is used in further calculations. It is a naturally iterative approach in which a value is obtained via a convergence of the system. The disadvantage of this kind of calculation is that it by nature neglects interactions, however it does allow a calculation of a macroscopic quantity. The mean field approximation is used in this work as a method of calculating the magnetic properties of the spins and is explained in greater detail in the following section.

2.3 Numerical Calculation of the $LiHo_xEr_{1-x}F_4$ System

2.3.1 Mean Field Approximation

As the Hamiltonian for the spins is a coupled many bodied operator, it is desirable to simplify it to allow for calculations. The approach used is known as the mean field approximation. In this approximation, the correlated fluctuations of the moments around their equilibrium position are ignored, which is achieved by expanding the $\mathbf{J}_i \cdot \mathbf{J}_j$ term as follows:

$$\mathbf{J}_i \cdot \mathbf{J}_j = (\mathbf{J}_i - \langle \mathbf{J}_i \rangle) \cdot (\mathbf{J}_j - \langle \mathbf{J}_j \rangle) + \mathbf{J}_i . \langle \mathbf{J}_j \rangle + \mathbf{J}_j . \langle \mathbf{J}_i \rangle - \mathbf{J}_i . \langle \mathbf{J}_j \rangle \tag{2.8}$$

The mean field approximation consists of neglecting the first term of this expansion (which is associated with two-site fluctuations), effectively decoupling the Hamiltonian to a sum of N independent terms for the single sites. The new Hamiltonian can then be solved for each magnetic ion relatively easily, however as the solution is dependent on the input, the routine must be iterated until self-consistency is achieved. The mean field calculation allows for the determination of various physical properties which can then be measured. In this case the values of $\langle \mathbf{J}_i \rangle^2$ were calculated, where i is the z-direction for Ho (Ising axis) and x-direction for Er (antiferromagnetic plane) ions. The choice of $\langle \mathbf{J}_i \rangle^2$ follows from the fact that this variable can be obtained through neutron scattering measurements which are discussed in Chapter 4.

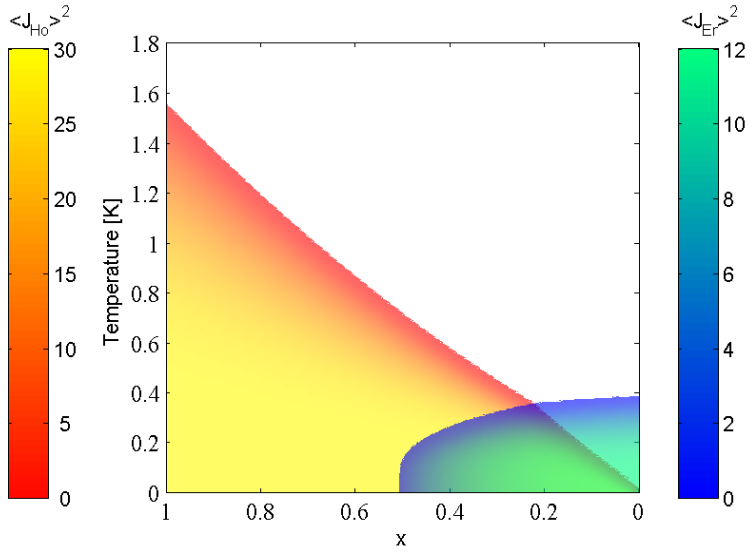

Figure 2.1: Phase diagram of $LiHo_xEr_{1-x}F_4$ calculated as a function of x. Colour scale shows the expectation value of the spin squared $< J >^2$ for the Holmium ions (red-yellow) and Erbium ions (blue-green)

2.3.2 Virtual Crystal Approximation

A complication of the $LiHo_xEr_{1-x}F_4$ system is that it is necessary to evaluate the Hamiltonian for two different ions which should be randomly placed at the magnetic sites. The most desirable way to do this is to set up a program which contains many sites which are populated at random and then calculate the mean field Hamiltonian. The downside to this approach is that once again the problem begins to become very large as the number of ions in the crystal is increased. Having a large number of sites is of course necessary to obtain a real random positioning of the ions.

Another approach is known as the virtual crystal approach. In this method, the mean field Hamiltonian is evaluated for both species of ions and then the two are combined in the correct proportions. This method is relatively simple and does not require much more computing time than a mean field calculation for a single ions type. The downside of this approach is that the nearest neighbour is always considered to be of the same species during the mean field calculation, which could lead to inaccuracies in the predictions.

2.3.3 Zero Field Calculations

The first calculation which is desired for an unknown system is to determine if there is any magnetic order or not. In the case of $LiHo_xEr_{1-x}F_4$, this is already known for $x = 0$ and $x = 1$. For $x = 0$ the system is an x-y antiferromagnet, with order occuring in the a-b plane, and for $x = 1$ an Ising ferromagnet is achieved with the Ising axis along the crystallographic c axis. In between these two points one would expect therefore a region

where the order is dominated by the ferromagnetic Ho ions and another region where the antiferromagnetic Er ions dominate. At some point where the interactions of both the Er and Ho are on the same level, there could be a cross-over region or even a completely different magnetic state.

Therefore the initial calculation on this system is a phase diagram as a function of x. Due to the virtual crystal approach, the way this is done is by showing the moment of the Ho ions along the c axis and the moment of the Er ions along the a-axis. Figure 2.1 shows the phase diagram which was calculated for $LiHo_xEr_{1-x}F_4$ as a function of x. The y axis of the graph gives the temperature of the system in K and the colour axis displays the moment squared ($\langle \mathbf{J} \rangle^2$). The yellow-orange colour represents the Ho ions and the blue-green colour that of the Er ions.

As the ordering temperatures of both $LiHoF_4$ and $LiErF_4$ are well documented, the data on this figure has been rescaled using a linear interpolation between $x = 1$ and $x = 0$. The scaling factor is the temperature measured experimentally divided by temperature obtained from the calculation. Without the scaling, the ordering temperatures at $x = 1$ and $x = 0$ are found to be about 30% higher than those measured experimentally. The phase diagram shows several areas where the magnetic properties of the system would be expected to be different.

Starting from $x = 1$ and going down to $x \approx 0.5$, the system is expected to behave as a dilute Ising ferromagnet as this is the behaviour typically seen in $LiHo_xY_{1-x}F_4$ [24] and the Er ions do not yet seem to begin to order. Seeing a re-entrant spin glass state would not be a surprise, even at large x, as the point of doping with Er is to increase off-diagonal interactions, adding frustration. On the other end of the composition, for sufficiently low x, between $x = 0.4$ and $x = 0.1$, the system is expected to behave as an antiferromagnet. The area in between the two is where it is not very easy to predict how the system will behave magnetically as the Ho and Er moments are of the same order.

Turning back to the calculation; it is interesting to compare how the order forms for various concentrations. This could give some insights into whether or not the mean field calculation continues to work in a reasonable manner. Figure 2.2 shows on the left the expectation value of the spin squared as a function of temperature for several compositions and on the right the same data normalised to the ordering temperature and the maximum obtained $\langle \mathbf{J} \rangle^2$. Both T_{Curie} and T_N were calculated by fitting the data for each concentration to a power law where $y = 0$ for $x > x_0$. This is of course the kind of curve observed in Figure 2.2, and therefore T_c is the temperature where $\langle \mathbf{J} \rangle^2$ begins to follow a power law. Starting with the normalised data, it is clear that the mean field calculation is consistent. This can be said, as the form for all concentrations is identical for both the Er and Ho ions.

Looking at the left hand graph, more insights into the possible behaviour of the system

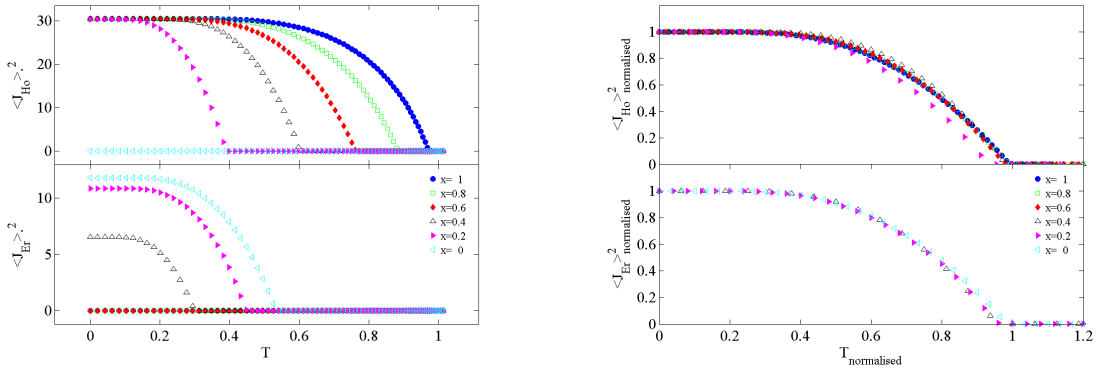

(a) (b)

Figure 2.2: (a) - $\langle \mathbf{J} \rangle^2$ as function of temperature for x = 0, 0.2, 0.4, 0.6, 0.8, 1 and (b) Normalised against $\langle \mathbf{J} \rangle^2$ and T_{Curie} for Ho and T_N for Er.

can be obtained. It seems that the Ho moments always order to give the same expectation value every time. This would imply that at a sufficiently low temperature all the Ho ions should align ferromagnetically. On the other hand, the Er ions behave differently, with the magnitude of the spin depending on the concentration of Er. This could mean that as the amount of Er is decreased, not a all of these moments will align anti-ferromagnetically into the plane. This could be an indication that instead of finding long-range antiferromagnetic order, anti-ferromagnetic clusters form in a paramagnetic/ferromagnetic background. In any case it certainly seems very probable that the Er moments will indeed aid in the formation of a spin glass state.

2.3.4 Calculation in Magnetic Field

To apply a magnetic field in the calculation, the field vector must simply be given in the Zeeman term. Due to the model example of a quantum phase transition which $LiHoF_4$ gives, it is interesting to see the effect of doping with Er on this transition. The calculations in this case attempt to see the ordering behaviour as a function of field, rather than that of temperature. As the Ho and Er moments are in theory perpendicular, calculations must be performed with fields along both the a and c axes.

2.3.4.1 Field along the a axis

As the Ho moments are considered to be more interesting in the presence of a magnetic field, the calculation is first done along the a axis. The calculation outputs a very large amount of data in this case, as essentially a Temperature field phase diagram is calculated for each concentration studied. A typical example of this phase diagram is shown on the

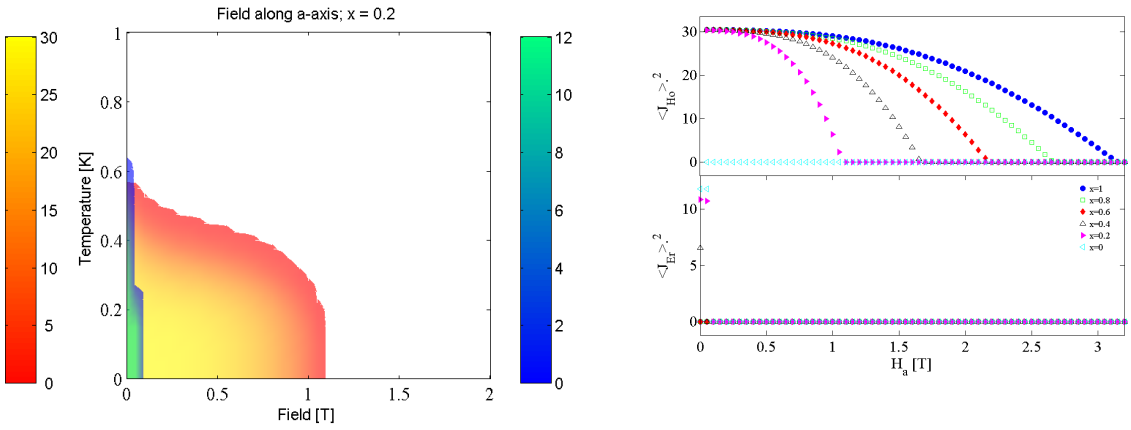

(a) (b)

Figure 2.3: (a) Phase diagram of $LiHo_{0.2}Er_{0.8}F_4$ as a function of H ∥ a. (b) $\langle J \rangle^2$ at T = 0 K as a function of H ∥ a for x=0, 0.2, 0.4, 0.6, 0.8, 1

left in Figure 2.3.

The composition used for this phase diagram is $LiHo_{0.2}Er_{0.8}F_4$, as both the behaviour of Ho and Er ions can be seen. As is expected, the application of a the field destroys the ferromagnetic order of the Ho ions aligned along the c axis. The field also destroys any antiferromagnetic order along the a axis. This is a particularity of the way the the calculation takes place. As in an antiferromagnetic order, the overall spin should be zero as the spins pointing along opposite directions should cancel out. For this reason, the Er order is calculated in an antiferromagnetic fashion, that is to say the spins at different sites are added together in an anti-parallel fashion. Therefore, when the antiferromagnetic order is destroyed, it says nothing about the possibility of it being replaced by a ferromagnetic order along the a axis.

On the right side of Figure 2.3 a similar graph to Figure 2.2, where the expectation value of the spin is graphed as a function of temperature, is shown. In this case however, the temperature is set to 0 K and the x axis is the field applied. The graph shows that as x is decreased, H_c decreases linearly as a function of x.

2.3.4.2 Field along the c axis

Applying the field along the c axis leads to some slightly different results as is seen in Figure 2.4. Once again, the phase diagram for $LiHo_xEr_{1-x}F_4$ where x = 0.2 is shown on the left and a comparison of different concentrations is on the right. From the phase diagram, it is clear that the Ho moments are essentially always aligned along the Ising axis. At low temperatures, one would not expect the field to change anything as the spins are already fully aligned. This image is shown very well in Figure 2.4 (b) - for all

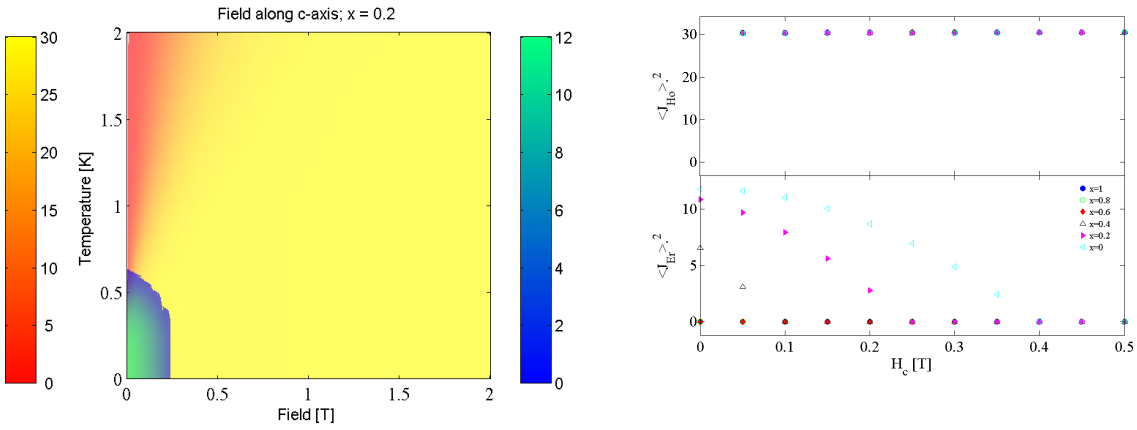

(a) (b)

Figure 2.4: (a) Phase diagram of $LiHo_{0.2}Er_{0.8}F_4$ as a function of H ∥ c. (b) $\langle J \rangle^2$ at T = 0 K as a function of H ∥ c for x=0, 0.2, 0.4, 0.6, 0.8, 1

concentrations of Ho, the ions are always aligned along the c axis at zero temperature in H_c. At temperatures higher than T_c on the other hand, the field should help to remove the thermal fluctuations and order the spins once again.

Looking at the Er ions, things go once again as is expected. The phase diagram shows that applying the field along the c axis destroys any antiferromagnetic order. The comparison of phase boundaries for different x confirms this picture. It is interesting to note that along the c axis, H_c is somewhat larger than along the a axis. This is in agreement with results taken on $LiErF_4$ which show $\frac{H_c \| c}{H_c \| a} \sim 3$ [14].

3 AC Susceptibility

The magnetic susceptibility χ is a measure of the systems ability to respond to an external DC field H. It is defined as

$$\chi = \frac{M}{H} \tag{3.1}$$

where M is the magnetisation of the sample. In a standard DC susceptibility measurement, the field remains constant, and the sample is slowly moved in and out of the field and the magnetisation measured. When measuring the AC susceptibility, the situation is somewhat different. The AC susceptibility measures the systems ability to respond to a small oscillating field H_{AC}, and χ_{AC} is defined as follows:

$$\chi_{AC} = \frac{dM}{dH} \tag{3.2}$$

Thus the susceptibility is actually the gradient of the magnetisation vs field curve which would typically be measured with a magnetometer. The appeal of the AC susceptibility technique is the ability to measure the frequency dependence of the susceptibility at any DC field (including ∼zero field). This is particularly useful when dealing with systems containing some short range order, such as spin glasses. In such systems the AC susceptibility allows a probe of the relaxation times involved, which can be used to determine the type of short range order of the magnetic moments.

3.1 Theory

To briefly outline the theory of what is being carried out in an AC susceptibility measurement, we start by taking an AC field, $H_{AC} = H_{AC0}\cos\omega t$, applied to the sample. The result of this field is to create a local flux density B inside the sample which has a phase lag relative to the original field H_{AC}. As B will be nonlinear, it can not be expressed as a sinusoidal function, therefore the average local flux density $\langle B\rangle$ must be described by a Fourier expansion:

$$\langle B\rangle = \mu_0 H_{AC0} \sum_{n=1}^{\infty} \left[\mu_n^{'}\cos(n\omega t) + \mu_n^{''}\sin(n\omega t)\right] \tag{3.3}$$

where $\mu^{'}$ and $\mu^{''}$ are the real and imaginary parts respectively of the complex magnetic permeability. Using the fact that the magnetic permeability and susceptibility are related by

$$\mu = 1 + \chi \tag{3.4}$$

the real and imaginary complex susceptibilities can be defined as follows (see [19] for a detailed derivation):

$$\chi_1^{'} = \left(\frac{\omega}{\pi \mu_0 H_{AC0}} \int_0^{2\pi/\omega} \langle B \rangle \cos(\omega t) dt \right) - 1 \tag{3.5}$$

$$\chi_1^{''} = \left(\frac{\omega}{\pi \mu_0 H_{AC0}} \int_0^{2\pi/\omega} \langle B \rangle \sin(\omega t) dt \right) \tag{3.6}$$

From these two expressions it is clear that the susceptibility gives a quantitative measure of the magnetic flux inside the sample. A quick calculation shows that in the case of complete penetration, $\chi^{'} = 1$ and for a complete Meissner expulsion $\chi^{'} = 0$. Similarly, for a superconducting state (Meissner expulsion) $\chi^{''} = 0$ and for any other state χ'' reflects the AC losses and is a small number (< 1).

The idea behind an AC susceptibility measurement is to induce an oscillating field into the sample by using a coil. The response from the sample is them measured with a second inductive coil. Typically either a third coil, or an additional set of coils are used to cancel out the original induced field H_{AC0}, giving a measurement purely of susceptibility of the sample.

3.2 Experimental Setup

For a AC susceptibility measurement, a field H_{AC} is induced by driving an AC current through what is known as the primary coil. The effect of this field is to produce a voltage in the secondary coil which has a frequency ω and is given by $V_{vacuum} = NA\mu_0 H_{AC} \sin(\omega t)$, where N is the number of turns in the coil, A is the cross-section and μ_0 is the vacuum permeability. In addition to this signal, the susceptibility of the sample, χ_{sample}, will create a voltage V_{sample}, leading to a total signal given by [20]

$$\begin{aligned} V_{Total} &= V_{vacuum} + V_{sample} \\ &= NA\mu_0 \sin(\omega t) + \chi_{sample} f_{sample} NA\mu_0 H_{AC} \sin(\omega t) \end{aligned} \tag{3.7}$$

where f_{sample} is a coupling constant. In our case, the secondary coil is approximately a long solenoid and thus f_{sample} represents the *filling factor*, the fraction of the volume of the secondary coil which is filled by the sample. V_{Total} along with its phase dependence can be measured with the help of a *lock-in amplifier*, in this case a Signal Recovery 7265. This

kind of measurement allows for the complex susceptibility of the sample to be deduced as long as one knows the phase of the AC current relative to the internal phase of the lock-in amplifier. Unfortunately, V_{sample} is often only a small contribution to V_{Total} and thus the coils must be designed in such a way as to minimise V_{vacuum}.

3.2.1 AC Susceptibility Coils

The coils used for the AC susceptibility measurements were manufactured by Cambridge Magnetic Refrigeration (CMR). They are of a concentric design, meaning that three coils are wound one on top of the other. The outermost coil is the primary coil and the two inner ones are the secondary coils (let us label them A and B) as is shown in Figure 3.1. The secondary coils are connected in an A-B configuration, which implies that the positive of coil A is connected to the positive terminal of coil B. In this configuration, the Voltages produced in the two coils will tend to cancel each other out. Due to the geometry of the coils (one coil is wound on top of the other), V_{sample} will be larger in one coil due to the larger filling factor. This allows for the signal arising from H_{AC} to be cancelled, leaving only the signal from the sample.

Of course, it is not normally the case that H_{AC} will be exactly cancelled out, and the coils will typically have to be modified slightly so that the difference between the two secondary coils perfectly cancels out H_{AC}. A current is run through the primary and the resulting background signal in the secondaries is measured. To ensure that the background is as small as possible, extra windings are added or removed from the outermost coil. Although the exact method used to balance the two secondary coils is unknown, the measured signal trough both coils is 0.9 % of the signal measured in one of the coils.

3.2.2 Cooling The Sample

Not only does the susceptibility of the sample need to be measured, but the temperature of the sample must be cooled to several tens of milliKelvin, and this temperature must be controlled accurately. To get the temperature down to ~25mK, an Oxford Kelvinox 25 dilution refrigerator is used.

The basic idea of a dilution refrigerator is that below temperatures of ~800mK a ^3He and ^4He mixture will undergo a phase separation. At this boundary, a quantum evaporation of ^3He takes place from a ^3He rich phase to a ^4He rich phase, which gives rise to a cooling power. The ^4He rich phase is in addition pumped on using a rotary vane pump and the gas is re-circulated into the system (for more information on dilution refrigerators see [8]).

The coldest point on a dilution chamber is known as the mixing chamber, as this is where the phase separation takes place, and it is to this copper plate where the sample

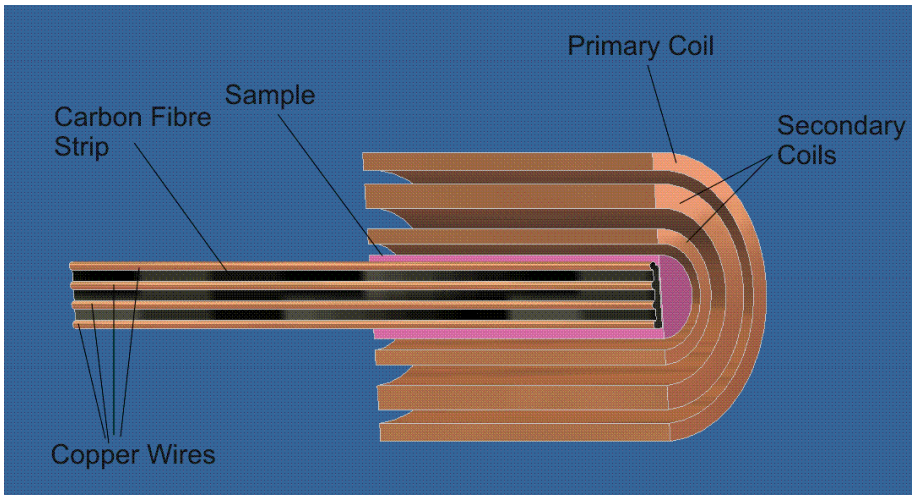

Figure 3.1: Diagram of the coils used for AC susceptibility measurements. The coils are mounted in Stycast epoxy and held in place with a Delrin plastic holder. The powder sample is mixed with Stycast and thermalised using 2-4 200 μm copper wires. The carbon fibre strip, which is attached to the Delrin holder ensures that the sample stays in the correct position throughout the measurements.

holder is attached. First, a so called weak-link is connected to the mixing chamber. The point of this weak link is to create a reasonable sized thermal mass whose temperature can be controlled independently of the mixing chamber. A thermometer and heater are attached to this copper thermal mass at the bottom of the weak-link. It is desirable to do this as an accurate control of the mixing chamber temperature is difficult due to different cooling characteristics at different temperature ranges. In particular, it is extremely difficult to control the temperature of the mixing chamber at temperatures above 1K as the two separate phases are destroyed.

After the weak link, Delrin plastics are used for all the structural pieces. The reason why metals are no longer used is that when ramping a DC field, eddy currents will be created inside any conductor, which will heat them. Using a plastic however will not have this effect and therefore ramping a magnetic field has very little effect on the temperature of the surroundings. The susceptometer coils are placed inside a piece of Delrin which effectively holds them in place as is shown in Figure 3.2. The photo also shows that the sample is attached to the plastic piece using a carbon fibre rod.

3.2.3 The Sample

Before discussing the sample used for the measurements, it is necessary to discuss briefly the advantages and disadvantages of using a powder versus a single crystal. Ideally, all measurements would like to be done on an aligned single crystal, as this will allow any quantum phase transitions as a function of field to be probed (i.e using a field transverse

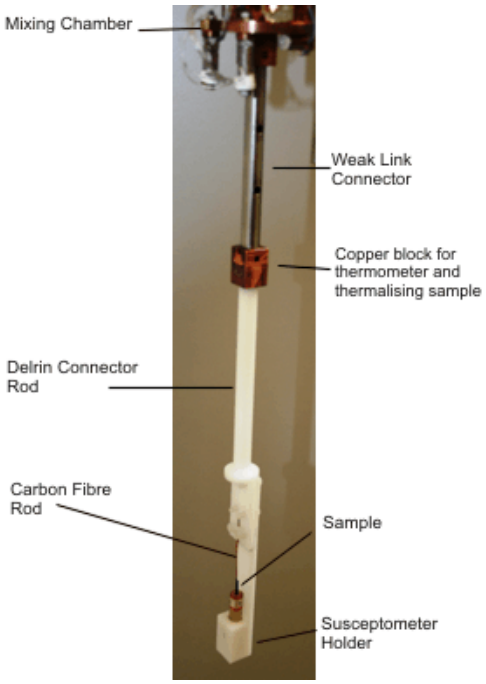

Figure 3.2: Photo of the susceptometer attached to the mixing chamber. The susceptometer sits in a Delrin holder which is attached to the weak link. The sample is thermalised by 200 μm diameter copper wires which are screwed down onto the copper piece of the weak link.

to the Ising axis). The downside with using crystals is that first a single crystal of a large enough size needs to be aligned and cut into a suitable sample. Typically when using a single crystal, the filling factor of the coils will be relatively small, leading to weaker signals. On the other hand if a powder is used, it is much easier to increase the filling factor. Powders also do not need to be aligned or cut, meaning that preparing a powder sample is much faster than for a single crystal. The downside to using a powder sample is that the field dependence of the sample can't be measured, as each individual grain of powder would be randomly aligned.

The samples which AC susceptibility measurements are carried out on consist of powders ground from crystals of $LiHo_xEr_{1-x}F_4$ which are mixed with an epoxy resin called Stycast 1266 epoxy. In addition to this mixture of Stycast and sample the carbon fibre rod is set along with 2-4 200 μm diameter copper wires. The wires are used as the thermal contact between the weak-link thermal mass and the sample. These wires are then clamped down between two copper washers onto the bottom weak-link to ensure as good a thermal contact as possible.

3.3 Determination of the Ordering Temperature

As $LiHo_xEr_{1-x}F_4$ is a new compound in the sense that it has never been measured before, the first aim of any experiment is to see if it behaves in a similar way to our expectations. As the anisotropic g-factor for the Ho ions is much larger than that for Er, the initial expectation is that the system should behave in a manner similar to $LiHoF_4$. This means that the system is expected to be paramagnetic at high temperatures and at low temperatures is expected to order ferromagnetically [10]. From the experiments done on $LiHo_xY_{1-x}F_4$, it would also seem likely that for small quantities of x, the system after becoming ferromagnetic, would at some lower temperature become a spin glass.

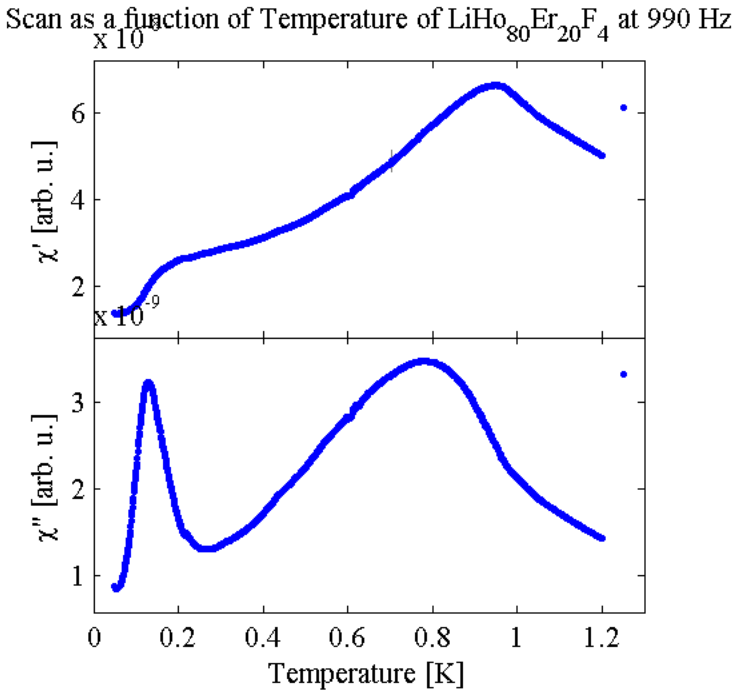

Figure 3.3: Typical AC susceptibility temperature scan. The high temperature peak in χ' corresponds to the system ordering, most likely ferromagnetically and the peak at low temperature in χ'' could correspond to the system freezing into a spin glass.

Therefore the first experiments are simple temperature scans of $LiHo_xEr_{1-x}F_4$ for the different percentages of x available. A temperature scan implies that the AC susceptibility is measured using a single excitation frequency and current while the temperature is slowly ramped up. A current of 10 μA is used as this corresponds to the largest obtainable current without a noticeable inductive heating effect; this current corresponds to a primary field H_{AC} of 42 mOe. As it likely that this system exhibits some glassy behaviour, for all scans the sample is cooled down to base temperature and then the susceptibility is measured

while warming the sample, removing any possible memory effects which may be observed. The sample is warmed at a rate of 0.2 mK / 10 sec from base temperature (typically $\sim 30-40$ mK) up to 250 mK and then at a rate of 1 mK / 10 sec for higher temperatures. A typical scan is shown in Figure 3.3, which shows a temperature scan for $LiHo_{0.8}Er_{0.2}F_4$.

The first feature in this scan is the peak in χ' seen at T = 950 ± 20 mK, which corresponds to the system 'ordering' from the paramagnetic state. This peak in the real signal also corresponds to the knee seen in the imaginary signal, which may in certain situations be better suited to determining T_c. The choice of which feature to use is fairly arbitrary, and in essence depends on which feature is the sharper of the two. Due to the complexity of the spin arrangement present in this system, the AC susceptibility data is unable to determine the kind of ordered state which is formed, although it seems safe to say that it is most likely ferromagnetic order. From this scan alone, it is also not possible to tell whether the system has truly formed a long-range ordered state or merely a state which has short range correlations. To determine whether the order is long or short range, the frequency dependence of the ordering Temperature must be studied, which is done later on.

The second feature in the scan is the rather sharp peak observed in χ'' seen at a temperature of 128 ± 5 mK. Although from this scan alone, not a very large amount of information can be gained from the existence of this peak, it suggests that after the state has ordered, something else happens to it. Once again, from the results already obtained on the $LiHo_xY_{1-x}F_4$ series it seems reasonable to think that this peak could correspond to a re-entrant spin glass state being formed. This single scan does certainly show that the low temperature magnetic properties of this particular composition are not what one would expect for a pure Ising ferromagnet.

It is useful to give a quick comparison of the features seen in the different concentrations of Ho before carrying on further. Figure 3.4 is a comparison of the different compounds measured. All scans were taken using a frequency of 990 Hz, allowing for a true comparison of the features. In this figure, the curves have all been normalised to give the same peak intensity. Although the absolute susceptibility wouldn't necessarily be the same for all peaks, it does make a comparison of the different curves much easier.

Another reason why this was done is that the mass of the samples is not accurately known, and indeed when using a powder it is very difficult to know. When mixing the powder with the Stycast, a reasonable (~20%) amount of the sample is stuck to the other materials used in the preparation of the sample. Although it is possible to measure the masses of all objects which came in contact with the mixture and the initial and final masses of both the sample and Stycast, the errors would be considerable. In addition to this, the sample is made 20 mm long, compared to 10 mm long coils, and it is not certain that the mixture once dry is homogeneous. Therefore even if the total mass of

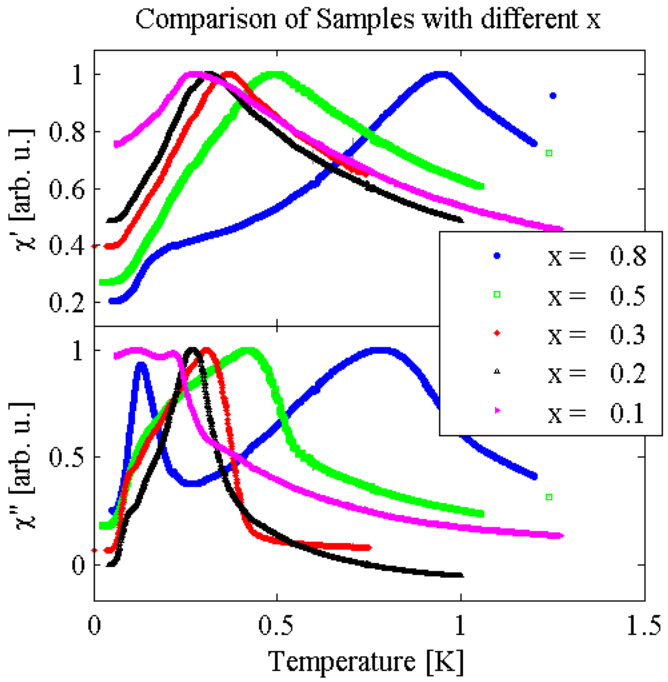

Figure 3.4: Comparison of the Susceptibility scans for varying concentration of Holmium x. All scans were taken at 990 Hz which allows for features with a frequency dependence to be compared.

Concentration of Holmium	1	0.80	0.50	0.30	0.20	0.10	0
Ordering Temperature [K]	1.53	0.95	0.50	0.37	0.31	0.28	0.38

Table 3.1: Ordering temperature of $LiHo_xEr_{1-x}F_4$ as function of x

powder in the sample is known, it would not necessarily be possible to say that half of this mass is being measured. As the samples almost certainly have different masses, any kind of comparison of relative amplitudes would most likely say more about the mass of the sample than the physics going on inside it. From these scans T_c was determined by finding the temperature at which the peak occurs in χ', and is shown in Table 3.1.

The obvious piece of information which comes from the curves is that the ordering temperature decreases with x. This is what is predicted by the mean field calculations. It is somewhat interesting that even at $x = 0.1$ the ordering temperature continues to decrease, as with such a large amount of Er in the crystal it would be reasonable to think that it was the Er moments ordering. Apart from the temperature dependence of T_c, it can be seen that the possible spin glass state is only present in the $x = 0.8$ sample. This is somewhat surprising, as in $LiHo_xY_{1-x}F_4$, the spin glass state persists for fractions of Holmium down to even $x = 0.045$ [22]. Finally it can be seen that for the $x = 0.2$ and $x = 0.3$ samples there is a knee in χ'' at T $\sim$ 100 mK, which could possibly indicate an entry into a spin glass state. Several of the compositions are studied in greater detail in Section 3.5.

3.4 Phase diagram

As this system is assumed to follow a somewhat mean field behaviour, it is desirable to compare the ordering temperatures with the mean field calculations. Due to the fact that the mean field calculation used ignores interactions between different species of ions, obviously some variations from the theory are expected. From the mean field calculations, an ordering temperature can be obtained by looking at the temperature when the moment begins increasing. A phase boundary is therefore calculated as the ordering temperature for different fractions of Ho. This prediction is then easily compared with the susceptibility measurements determining the ordering temperature, and is done in Figure 3.5. It should be noted that in this figure, the ordering temperature is determined from temperature scans taken using a driving frequency of 990 Hz.

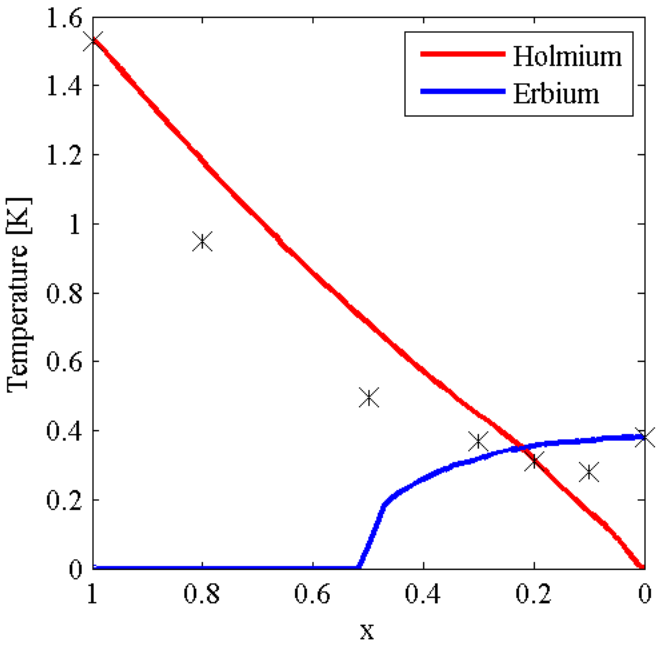

Figure 3.5: Comparison of mean field calculated phase diagram with experimental data. The data points (crosses) are all taken at a frequency of 990Hz in case the order does not correspond to long range order and will thus show a frequency dependence.

As both $LiHoF_4$ and $LiErF_4$ are well characterised, the theoretical phase diagram is scaled such that the ordering temperatures for x=1 and x=0 are correct. The method used to do this is the same as previously discussed in Section 2.3.3. It is very easily seen that the theoretical ordering temperatures are higher the ordering temperatures measured. This does not come as much of a surprise as the situation is the same for $LiHo_xY_{1-x}F_4$, where mean field calculations show a phase boundary which is shifted too high in temperature [14].

3.5 Frequency Dependence

As has already been mentioned, one of the strengths of AC susceptibility measurements is the ability to probe the frequency dependence of a response. This is extremely useful as it allows for long range and short range order to be separated, and within this short range order, superparamagnets and spin glasses to be separated. Several different compositions of $LiHo_xEr_{1-x}F_4$ are measured in order to determine if any of the features seen in the temperature scans have a frequency dependence.

3.5.1 $LiHo_{0.80}Er_{0.20}F_4$

The sample which from the temperature scan shows the most promise of some kind of short-range ordered state is $LiHo_{0.80}Er_{0.20}F_4$ as there are two very obvious peaks at different temperatures. The frequency dependence in this case is determined by carrying out temperature scans at different frequencies, heating up above T_c between each scan in case there is any history dependence of the sample.

The temperature scans are taken at four different frequencies: 8.9, 77, 330 and 990 Hz and are shown in Figure 3.6. From the graph on the left, which shows the individual scans, several important observations can be made. These scans confirm that the system does indeed enter into a long-range ordered state at a temperature of 950 mK as the peak in χ' does not show a frequency dependence. This is more easily seen in the χ'' scan, where a kink is seen in the curve. This kink clearly has no frequency dependence and thus implies a long range order.

Moving on to the low temperature features, a frequency dependence is very evident. The peak seen below 150 mK in χ'' moves to lower temperatures as the frequency is decreased. This is expected in any kind of system where there is no long range order but instead clusters of an ordered state are formed, without creating an overall order. The frequency dependence of the system implies that once in the frozen state there is a distribution of relaxation times, due to the formation of clusters. The peak for a certain frequency is nothing more than the individual blocking temperature for clusters with the corresponding relaxation rate [18].

To determine what kind of clustering is formed is somewhat difficult as there is currently no theory which adequately explains the dynamics of spin glasses. One way which is very commonly used is to try fitting the data using Arrhenius law , which is the law used to describe superparamagnetism:

$$\tau = \tau_0 \exp(\frac{E_a}{k_B T}) \tag{3.8}$$

where E_a is an energy barrier separating two spin states, τ is the relaxation time, T is the temperature of the system and τ_0 is a microscopic limiting relaxation time. This can be rewritten as follows,

$$\omega = \omega_0 \exp(\frac{-E_a}{k_B T_{\mathrm{f}}}) \tag{3.9}$$

The data should fit for both a spin glass and a superparamagnet, however in the former case the fit parameters will be unphysical. Typically a canonical spin glass will find $\omega_0 \sim 10^{200}$ Hz and E_a equal to several thousand K. Another method which can be used to separate the kind of clustering formed is to look at the shift in T_{f} per decade of frequency, i.e.

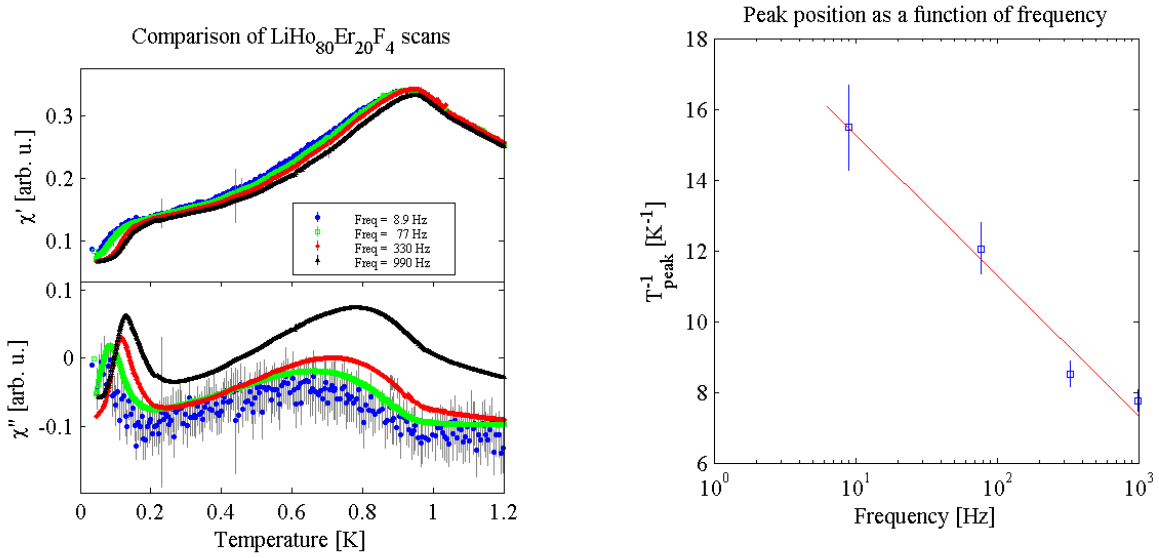

(a) (b)

Figure 3.6: Frequency dependence seen in the 80% Ho Sample. (a) shows separate temperature scans done at different frequencies, showing the difference in the peak position in χ''. (b) is a graph of $1/T_{peak}$ as a function of $\log(\omega)$. The fact that a straight line can be fit to this data shows that the data follows Arrhenius law.

$$\frac{\Delta T_{\mathrm{f}}}{T_{\mathrm{f}} \Delta \log(\omega)} \tag{3.10}$$

For a canonical spin glass the value is $\sim 10^{-4} - 10^{-3}$ and for superparamagnetism the value is $\gtrsim 10^{-1}$. Anything which falls between these two values is generally considered to be a spin glass of some kind. For $LiHo_{0.8}Er_{0.2}F_4$ it was found that $\frac{\Delta T_{\mathrm{f}}}{T_{\mathrm{f}} \Delta \log(\omega)} = 0.244$, which would imply that at this concentration the behaviour is more superparamagnetic. This means that although clusters do form, they do not have much of a collective behaviour and each cluster behaves as a single spin would do in a paramagnet.

3.5.2 $LiHo_{0.50}Er_{0.50}F_4$

A similar set of temperature scans was run on on the $x = 0.5$ sample. In this case an even lower frequency was used in an attempt to probe any frequency dependence with greater accuracy. From Figure 3.7 (a), a small frequency dependence can be seem in the peak in χ'. This immediately indicates that the system does not order ferromagnetically, and only forms into a clustered state. The frequency dependence of the T_{f} is shown in Figure 3.7 (b), and highlights one of the problems with the AC susceptibility method employed here.

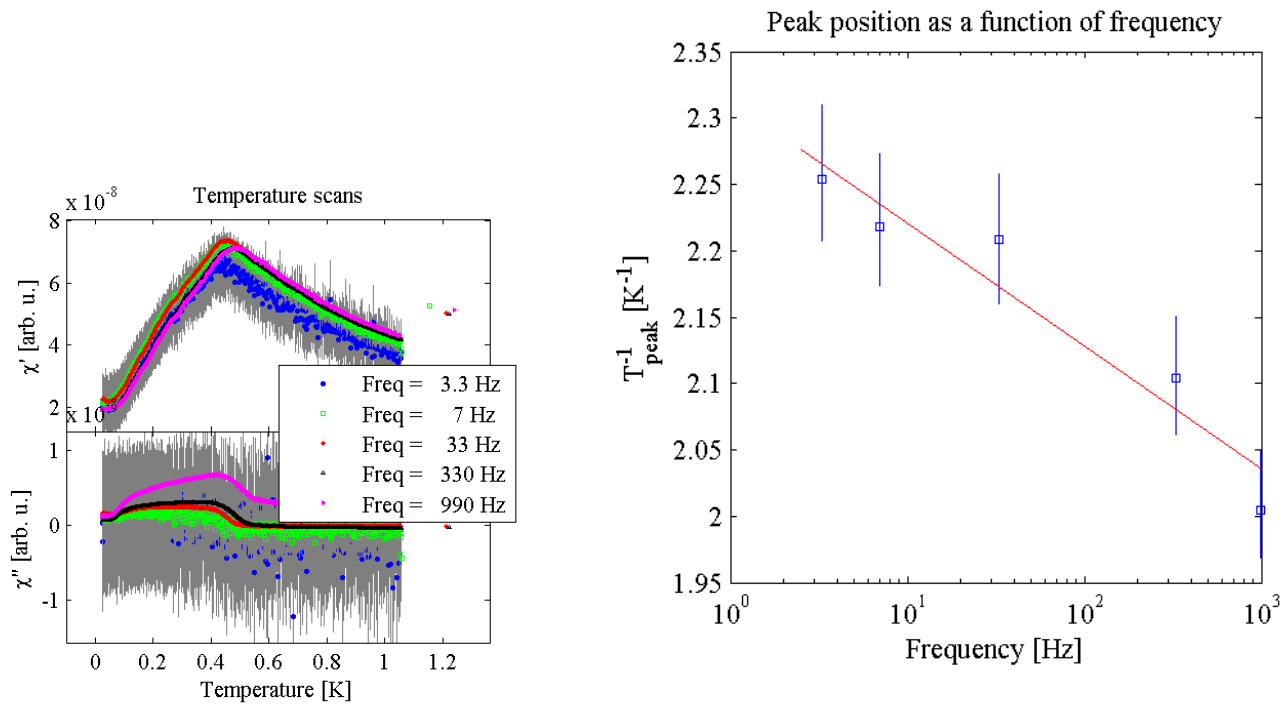

(a) (b)

Figure 3.7: Frequency dependence seen in the 50% Ho Sample. (a) shows separate temperature scans done at different frequencies, showing the difference in the peak position in χ''. (b) is a graph of $1/T_{peak}$ as a function of $\log(\omega)$.

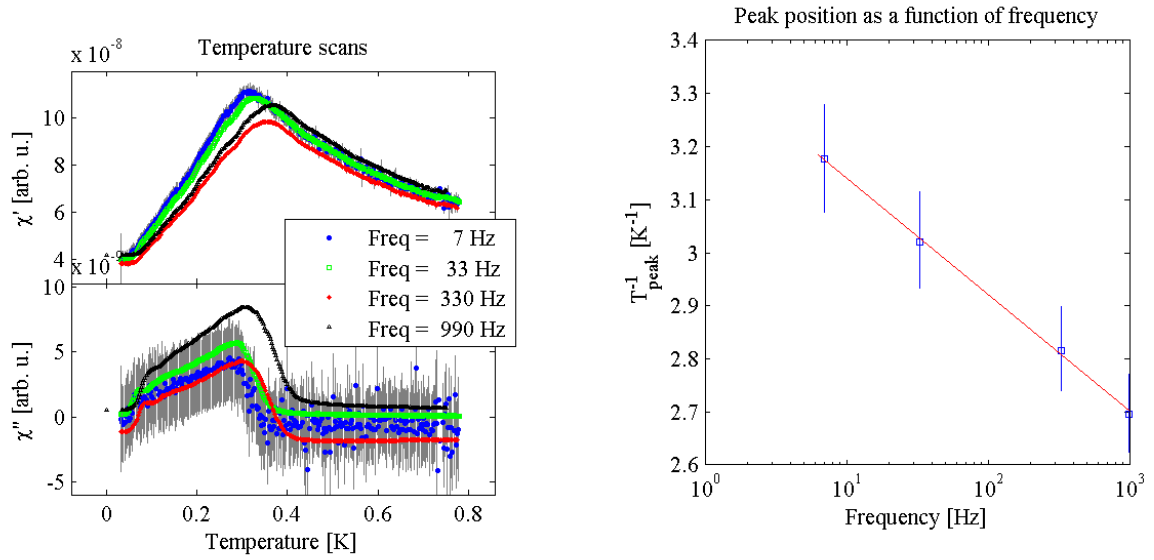

(a) (b)

Figure 3.8: Frequency dependence seen in the 30% Ho Sample. (a) shows separate temperature scans done at different frequencies, showing the difference in the peak position in χ''. (b) is a graph of $1/T_{peak}$ as a function of $\log(\omega)$.

It is found that $\frac{\Delta T_f}{T_f \Delta \log(\omega)} = 0.04$ in this case, which would imply that the system is some kind of a spin glass. Unfortunately, the seemingly small error in T_f of 10 mK on a temperature in the range of 400 mK, corresponds to a much larger error once the inverse is taken. This makes it difficult to truly determine the behaviour of the system. It still does seem likely that the behaviour is due to a spin glass as the shift in T_f is still much smaller than one would expect for a superparamagnetic system.

3.5.3 $LiHo_{0.30}Er_{0.70}F_4$

In the $x = 0.3$ sample, the picture is somewhat similar to the $x = 0.5$ sample, as there is still a small frequency dependence on the peak position. It is important in Figure 3.8 (a) to note that the signal has drifted somewhat. This can be seen by the difference in χ'' at temperatures above T_f. At these temperatures, the sample should behave paramagnetically only and therefore χ'' should be constant (and assuming there is no background from the coils, it should be zero). As this is not the case, the signal has drifted slightly. This is the reason why the peak at 330 Hz appears to have a lower intensity of that at 990 Hz.

The frequency dependence of the freezing temperature once again shows that there is a clustered behaviour, and as $\frac{\Delta T_f}{T_f \Delta \log(\omega)} = 0.07$, this behaviour is typical of a spin glass. Unfortunately, due to the uncertainty in the exact value of T_f, it is not possible to say if

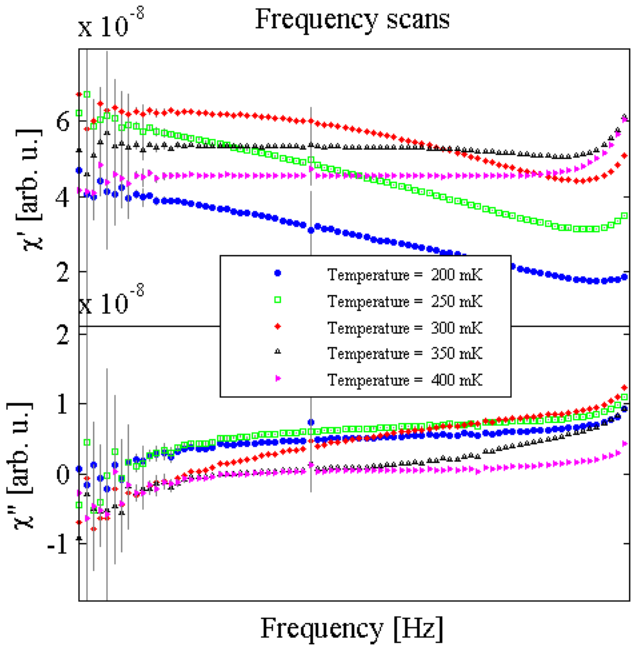

Figure 3.9: Frequency scans of $LiHo_{0.30}Er_{0.70}F_4$ at various temperatures around T_f, subtracted from a frequency scan taken at 1K. The lack of a peak in χ' most likely implies that the change in signal as a function of frequency around T_f is smaller than the instrumental resolution.

there is a distinct behavioural difference between this sample and the $x = 0.5$ one.

In order to try to improve the accuracy for the data used to calculate T_f, frequency scans can be used in addition to the temperature scans. The main advantage of doing a frequency scan is that it doesn't depend on the temperature of the sample changing as fast as the temperature of the thermometer. It is known from initial AC susceptibility measurements that the $LiReF_4$ is a good thermal insulator, meaning that the temperature of the sample takes much longer to change than that of the thermometer. Although care has been taken to go slow enough that there is not a large thermal lag between the sample and the thermometer, realistically, this can not be completely avoided. With a frequency scan on the other hand, the temperature is kept constant throughout the scan, meaning that there is no risk of a time lag on the response of the sample.

A selection of the frequency scans are shown in Figure 3.9. Frequency scans are carried out once again using a 10 μA driving current (corresponding to 42 mOe). In these graphs, a frequency scan at 1K has been subtracted from the data, as at this temperature it is assumed that the sample is in a paramagnetic state and should therefore not have a frequency dependence. The four scans chosen span the region where T_f is variable in the frequency range measured. As is the case in the temperature scans, a peak is expected

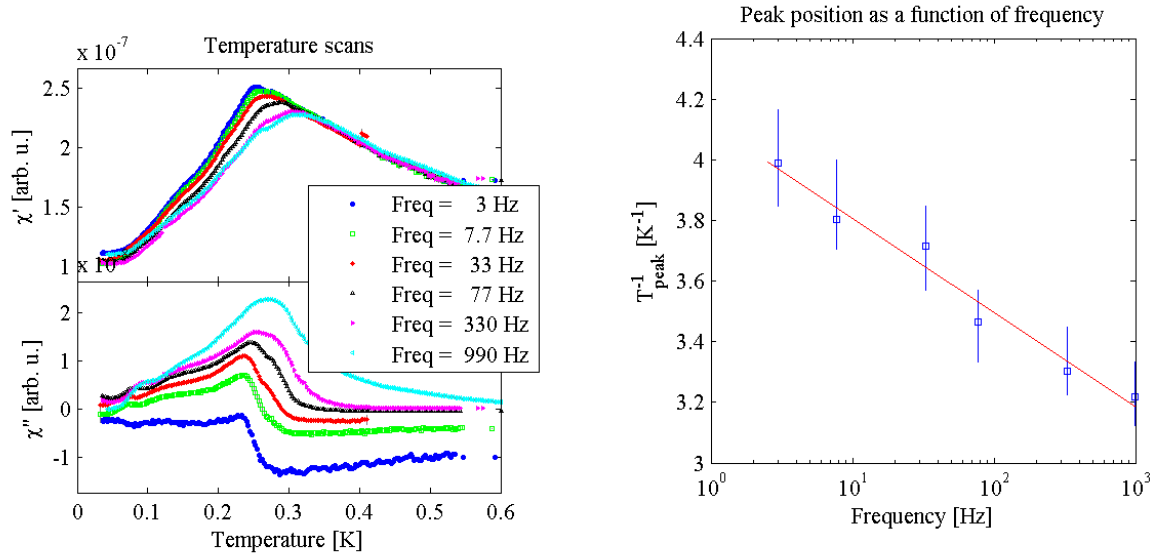

(a) (b)

Figure 3.10: Frequency dependence seen in the 20% Ho Sample. (a) shows separate temperature scans done at different frequencies, showing the difference in the peak position in χ''. (b) is a graph of $1/T_{peak}$ as a function of $\log(\omega)$.

in χ', which is not seen. It is not hugely surprising that there is not a visible peak in any of these scans, as the from the temperature scans (Figure 3.8 (a)) it can be seen that the intensity of the peak is almost independent of frequency and this peak is very wide. The lack of a peak in the frequency scans simply shows that the sensitivity of the measurement is not sufficient to make out the peak. The increase of signal as frequency decreases seen in 200 and 250 mK supports this image. At these temperatures, the peak is at a frequency well below 1Hz, and the increase in signal is due to the fact that at high frequencies the system is completely frozen, and the small field is not enough to excite the moments, where as at the lower frequencies the system can still be excited.

3.5.4 $LiHo_{0.20}Er_{0.80}F_4$

The final sample to be analysed at several frequencies is $LiHo_{0.20}Er_{0.80}F_4$. This composition behaves very similarly to the $x = 0.30$ compound, which is not very surprising. Analysis of the frequency dependence reveals a shift of $\frac{\Delta T_f}{T_f \Delta \log(\omega)} = 0.076$, which once again implies a spin glass state. In this case it also seems as if the system is behaving more like a canonical spin glass, as the intensity of the peak in χ' definitely increases as the frequency is decreased.

4 Neutron Scattering

Neutron scattering is a very powerful tool in solid state physics, and particularly when it is desirable to probe the magnetic properties of the sample. The reason why neutron scattering is so useful in quantum magnetism can be summarised as follows.

- The neutron has a spin and as such can interact with magnetic moments in the crystal, allowing measurements of both structural and magnetic properties.
- The energies of neutrons can be tuned relatively easily to what is known as the thermal range: $5 - 25$ meV. This corresponds to wavelengths of $2 - 4$ Å, which is comparable to the inter atomic spacing and also the correlation lengths of magnetic moments.
- Neutrons can penetrate deep into matter due to their uncharged nature, allowing for bulk measurements instead of surface measurements.

The downside to neutron scattering is the relatively weak intensities of neutron sources, forcing long measurement times. There is also a difficulty in creating neutron sources, which require either a nuclear reactor or a spallation source, making neutron scattering much more expensive than most other probes of magnetic properties.

4.1 Theory

A neutron scattering experiment consists of shining a beam of neutrons in state $|\boldsymbol{k}, \sigma\rangle$ into a target which, through interactions, transforms this beam into the final state $|\boldsymbol{k}', \sigma'\rangle$. This interaction also transforms the target from an initial state $|i\rangle$ to the final state $|f\rangle$. A monochromatic beam is used which can be treated as a plane wave state $|\boldsymbol{k}, \sigma\rangle = \frac{1}{\sqrt{V}} e^{i\boldsymbol{k}\cdot r} |\sigma\rangle$. It is useful to define the following terms associated with a scattering process.

$$\text{Energy transfer}: \quad \hbar\omega = \frac{\hbar^2 k'^2}{2M} - \frac{\hbar^2 k^2}{2M} \tag{4.1}$$

$$\text{Wave vector transfer} \quad \boldsymbol{\kappa} = \boldsymbol{k}' - \boldsymbol{k} \tag{4.2}$$

Fermi's golden rule applied to the interaction Hamiltonian gives the probability of a transition of a neutron between the initial and final states:

$$W(\boldsymbol{k},\sigma;\boldsymbol{k}',\sigma') = \frac{2\pi}{\hbar}\sum_{if} P_i \left|\langle \boldsymbol{k},\sigma;i\left|\mathcal{H}_{int}\right|\boldsymbol{k}',\sigma';f\rangle\right|^2 \delta(\hbar\omega - E_f + E_i) \tag{4.3}$$

where P_i is the probability of a neutron being in the initial state. The scattering cross section is therefore:

$$\frac{d^2\sigma}{dEd\Omega} = \frac{k'}{k}\frac{M^2}{8\pi^3\hbar^3}W(\boldsymbol{k},\sigma;\boldsymbol{k}',\sigma') \tag{4.4}$$

where the fact that the incoming flux of neutrons in as state $\boldsymbol{k}$ is $\hbar k/VM$ and the number of neutrons in an energy interval dE centered around $\hbar^2k^2/2M$ is $\delta N = V/8\pi^3(Mk'/\hbar^2)$ has been used.

Neutrons can be either scattered by nuclei in the crystals or the spin of the neutron can interact with the electrons in the target. This leads to two separate cross sections, the nuclear and the magnetic cross section (for a derivation, see in particular [27]):

4.1.1 Nuclear cross-section

Nuclear scattering results from the periodicity of the nuclei in the crystal structure. There are two sources for the nuclear cross-section, the coherent-cross section:

$$(\frac{d^2\sigma}{dEd\Omega})_{coh} = \frac{k'}{k}\frac{1}{2\pi\hbar^2}\sum_{jj'}\bar{b}_j\bar{b}_{j'}\int\langle e^{i\boldsymbol{\kappa}.\boldsymbol{R}_j(t)}e^{-i\boldsymbol{\kappa}.\boldsymbol{R}_{j'}(0)}\rangle e^{-i\omega t}dt \tag{4.5}$$

and the incoherent-cross section:

$$(\frac{d^2\sigma}{dEd\Omega})_{inc} = \frac{k'}{k}\frac{1}{2\pi\hbar^2}\sum_{jj'}(\bar{b^2}_j - \bar{b^2}_{j'})\int\langle e^{i\boldsymbol{\kappa}.\boldsymbol{R}_j(t)}e^{-i\boldsymbol{\kappa}.\boldsymbol{R}_{j'}(0)}\rangle e^{-i\omega t}dt \tag{4.6}$$

where $\boldsymbol{R}_j$ is the position of the nuclei in the crystal and $\bar{b}_j$ is the average scattering length of the element at position $\boldsymbol{R}_j$.

The coherent cross-section is given by the average scattering length on each site and produces interference effect, while the incoherent scattering is due to the random variations of the scattering length and gives rise to a background signal.

4.1.2 Magnetic cross-section

The magnetic cross-section is much more complicated than the nuclear one and is given by:

$$\frac{d^2\sigma}{dEd\Omega} = \frac{k'}{k}(\gamma r_0)^2 \underbrace{\left|\frac{g}{2}F(\boldsymbol{\kappa})\right|^2}_{1} \underbrace{e^{-2W(\boldsymbol{\kappa})}}_{2} \underbrace{\sum_{\alpha\beta}(\delta_{\alpha\beta} - \hat{\kappa}_\alpha\hat{\kappa}_\beta)}_{3} \times \int dt\, e^{-i\omega t} \sum_{jj'} e^{i\boldsymbol{\kappa}(\boldsymbol{R}_j - \boldsymbol{R}_{j'})} \underbrace{\left\langle S_l^\alpha(0) S_{l'}^\beta(t)\right\rangle}_{4} \quad (4.7)$$

In this equation, there are several important factors.

1. The squared form factor $\left|\frac{g}{2}F(\boldsymbol{\kappa})\right|^2$, which describes the spatial distribution of the moments.
2. The Debye-Waller reduction factor $e^{-2W(\boldsymbol{\kappa})}$, which takes into account lattice motion that can transfer some of the coherent scattering into incoherent scattering.
3. A polarisation factor $\sum_{\alpha\beta}(\delta_{\alpha\beta} - \hat{\kappa}_\alpha\hat{\kappa}_\beta)$.
4. The spin correlation function $\left\langle S_l^\alpha(0) S_{l'}^\beta(t)\right\rangle$.

As can be seen from (4.7) a very useful aspect of neutron scattering is that it is possible to determine the spin correlations from the scattering cross-section.

4.1.3 Neutron Scattering experiments

In practice it is not possible to create the idealistic collimated and monochromatic beams which give rise to the cross-sections stated above. To understand any experimental results, these ideas must be abandoned and replaced with a finite distribution in both divergence and energy. This results in a measured intensity which is given by the convolution of the scattering cross-section and the experimental resolution, which can be written as:

$$I(\kappa,\omega) = \int \frac{d^2\sigma}{dEd\Omega}|_{\kappa',\omega'} R(\kappa,\omega;\kappa'-\kappa,\omega'-\omega)d\kappa' d\omega' \quad (4.8)$$

where $R(\kappa,\omega;\kappa'-\kappa,\omega'-\omega)$ expresses the probability that a nominal scattering condition specified by κ and ω will result in a measurement of a neutron with $\kappa' = \kappa + \Delta\kappa$ and $\omega' = \omega + \Delta\omega$.

4.2 Experimental Setup

The experiment consists of measuring a crystal of $LiHo_{0.25}Er_{0.75}F_4$ with the a-c plane in the beam line on a cold source triple axis spectrometer. The preparation of the sample and the RITA 2 spectrometer are briefly outlined in this section.

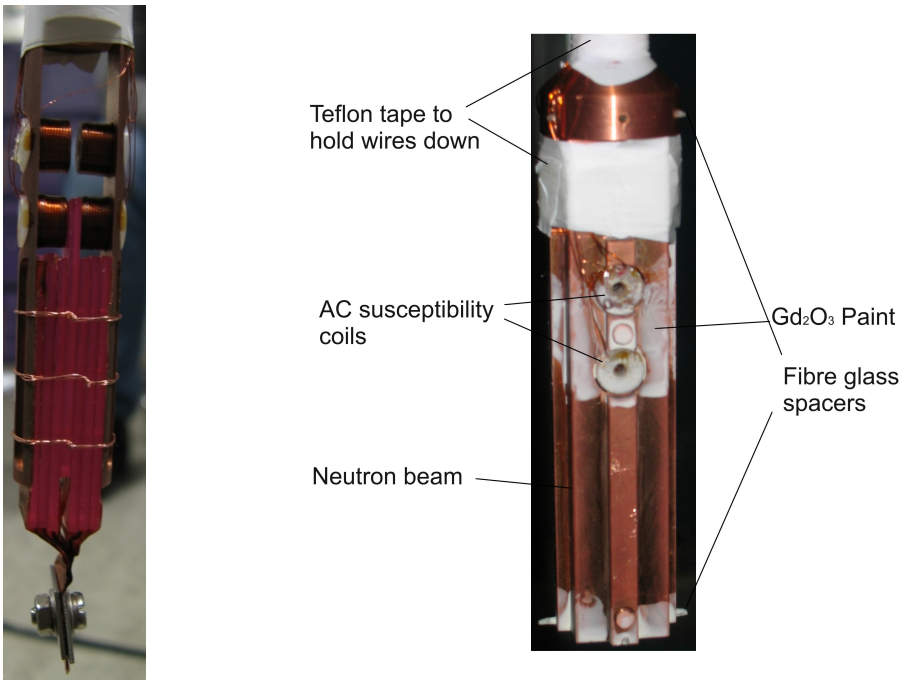

(a) (b)

Figure 4.1: Photo of the setup for neutron scattering measurements. (a) shows the a cross sectional view of the crystals and the susceptibility coils taken from an experiment on $LiHo_{0.33}Y_{0.67}F_4$. (b) shows the already mounted and closed sample holder used for $LiHo_{0.25}Er_{0.75}F_4$.

4.2.1 Sample Preparation

Due to the long and rather expensive nature of neutron scattering experiments, a lot of planning and care goes into the sample preparation. For the purposes of the experiments carried out, there are several key ingredients in the preparation of the sample, which are outlined in the folling sections. To make the description easier, Figure 4.6 shows on the left the cross-section of the crystal and AC susceptibility coils from a previous sample holder and on the right the assembled sample holder used for this experiment.

4.2.1.1 Maximum volume for the permitted sample space

The incoming beam of neutrons can be considered as a beam with a rectangular cross section whose height is 40 ± 5 mm and width is 20 ± 5 mm. To get the largest possible intensity of a diffracted beam, the initial beam must be filled as well as possible. The sample must be rotated to measure along different directions in reciprocal space, implying that a cylindical sample with a diameter of 20 mm would be ideal. As the probability of a neutron to interact with the sample is generally small, having a larger volume of sample which neutrons must traverse will increase the number of neutrons scattered. For these two reasons it is desirable to have a sample as large as possible. In the vertical direction,

there is no limitation, however larger than 40 mm would not gain anything. In the two horizontal directions, the size of the sample is limited by the inner vacuum chamber of the dilution fridge used as will be discussed later on.

4.2.1.2 Ensure good temperature control

A good temperature control is critical first of all understanding the data, and secondly comparing this data to that already discussed from the AC susceptibility technique. The first implication of this is that it is necessary to once again use a dilution refrigerator. Going from the mixing chamber to the sample, a solid copper rod is used and the sample is attached to this rod. At the same time, due to the fact that the sample is both a very good thermal insulator and also rather large, some means of thermalisation is needed.

To try to achieve a good thermalisation, the sample is cut into wafers measuring 30 x 12 x 1.4 mm^3. A total of seven of these wafers are used, leading to a sample measuring 30 x 12 x 9.8 mm^3. The wafer in the middle is cut to a length of 40 mm, which is positioned between the two sample coils to allow for the measurement of AC susceptibility. These thin wafers are then sputtered with 2 μm of gold, giving a good thermal contact between the layers. 30 μm copper foils are inserted between each layer of crystal and are thermally anchored to the copper bulk of the sample holder. This is achieved by running the foils along the entire length of the crystal at the bottom of the copper box. When the lid of the box is screwed down, the copper is pressed, leading to a good thermal contact.

The final key point in temperature control is to ensure that there are no large heat leaks towards the edge of the vacuum chamber of the dilution refrigerator. The environment around the sample holder is sitting in a vacuum and the tube which it is in has a diameter of 24 mm. As the sample holder is up to 20 mm wide, there is a risk of it touching the edge of this vacuum chamber. The walls of the vacuum chamber are at $\sim$2 K, therefore a touch between the wall and sample holder would effectively mean dilution temperatures could not be reached. To try to combat this problem, glass fibre spacers are placed around the top and bottom of the sample holder.

4.2.1.3 Keep the sample well fixed to the cold finger

As elastic neutron diffraction requires a single crystal (or several co-aligned single crystals), the application of a DC field now makes sense. The holmium ions in the crystal have a rather large moment ($\mathbf{J} = 8$), which in the presence of a field being ramped, produces a significant torque. In previous experiments, the sample has been ripped from the sample holder or the copper sample holder bent. For this reason, box made from 1 mm thick copper in two pieces, where one is a cavity much like a coffin and the other is a lid, is chosen as the sample holder. Each external face of the box has an extra 1mm thick

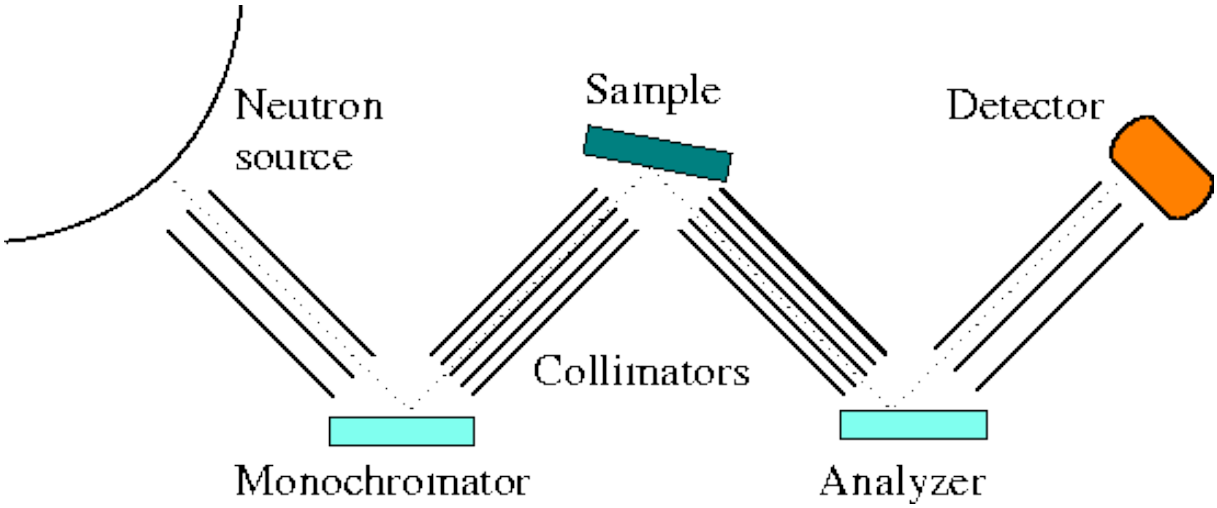

Figure 4.2: Schematic of a triple axis spectrometer such as RITA 2.

ridge to reinforce the structure. Due to the limited space, the internal cross-section of the sample holder is 12 x 12 mm^2.

4.2.1.4 Have the ability to measure AC susceptibility

In this experiment, an attempt is made to measure both the neutron scattering information and AC susceptibility at the same time. For this to be done, coils are needed which can be integrated into the sample holder. This is done as is shown in Figure 4.6 (a). In this image, four coils are visible, two at the top of the sample holder and two at the bottom. The two coils at the bottom shall be called the sample coils, as these measure the sample and the other two are the background coils, as they measure only the vacuum. In each pair there is a primary and secondary coil. The primary coils are visible and are wound out of a superconducting wire, to minimise any resistive heating. The secondary coils are underneath the primary ones and are wound out of 50 μm thick copper wires. As can be seen, the coils are split, meaning that each pair of coils is effectively a single coil with a gap in the middle.

4.2.2 RITA2

The measurements are carried out on the RITA2 triple axis spectrometer at SINQ of the Paul Scherrer Institut in Villigen, Switzerland. Before detailing the specifics of RITA2, the general concepts of a triple axis spectrometer (TAS) must be introduced. Figure 4.2 shows a general schematic of a TAS.

The key ingredients of a TAS are the neutron source, the monochromator, the sample, the analyser and the detector. The monochromator and analyser are typically a set of layered crystal planes separated by a spacing d and at an angle θ to the incoming beam.

Most of the neutrons in a white beam (i.e. a beam containing a large distribution in energies) will not meet the diffraction condition and will pass through these crystals. Neutrons which have a wavelength $\lambda = 2d\sin\theta$ on the other hand will be scattered with an angle of 2θ. Using this technique, a single energy of $E = \frac{h^2}{2m\lambda^2}$ is selected from the initial white beam. As the sample is placed between the monochromator and the analyser, $\boldsymbol{k}_i$ and $\boldsymbol{k}_f$ are both well defined for the scattering. The monochromator, sample and analyser each represents an axis of rotation leading to the name of a triple axis spectrometer.

Moving on to the setup used on RITA2, the incoming neutrons are produced by spallation and pass through a cold source. The monochromator consists of 9 pyrolytic graphite (PG) crystals which allow for a vertical focusing of the neutron beam. Before and after the sample there are motorised slits made of 10 mm thick BN plates which are used to further collimate the incoming and outgoing neutron beam. In front of the analyser, a BeO filter is used to attenuate neutrons from higher order diffraction. The analyser consists of 7 PG blades, which give the opportunity to measure slightly different $\boldsymbol{k}_f$ vectors simultaneously. The detector used is a $30 \times 50\,cm^2$ position sensitive detector which has an effective 128×128 pixels. For more information on the RITA2 spectrometer, please consult [12].

The sample is mounted inside a dilution refrigerator which is inside a cryostat designed specifically for neutron scattering. The cryostat used contains a 1.8 T horizontal split coil superconducting magnet. The sample is mounted inside the dilution fridge such that the a-c plane is horizontal. The cryostat itself is bolted onto the sample table and through a motorised goniometer can be tilted several degrees to ensure that the neutrons scatter in the a-c plane. Due to a mechanical limitation of the goniometer, it was only possible to use a magnetic field of up to 1 T.

4.3 Results and Discussion

Due to the relatively unknown system and possible complexity of the system. The experiment consisted of finding any magnetic order and attempting to determine its temperature and field dependence. The field dependence is investigated with the field pointing along the c-axis of the crystal. The first results to be presented are those relating to ferromagnetic order.

4.3.1 Ferromagnetic Correlations

A technical difficulty for determining if there is any ferromagnetic order is that this order will be present at the same reciprocal space as the nuclear Bragg peaks. In the case of a long range ferromagnetic order, the peak, which due to the resolution of the detector

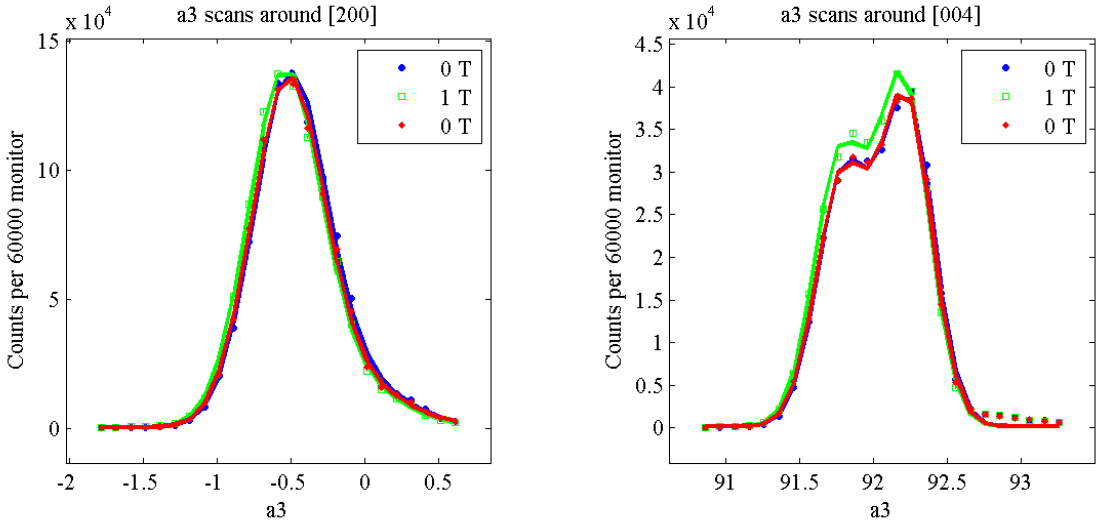

(a) (b)

Figure 4.3: Field dependence of the (a) (200) and (b) (004) Bragg peaks. The scans are taken in zero field, then with a field of 1 T then at zero field once again to try to determine if any hysteresis is present.

is a Gaussian, should simply gain intensity. If on the other hand, there are short-range correlations, the peak will become the convolution of a Gaussian with a broad Lorentzian.

The way any kind of order is searched for is by scanning around a nuclear Bragg peak at different temperature and fields. The three main places where this should be done is at high temperature and zero field, base temperature and zero field, and finally base temperature in a large field. In this case high temperature is taken to be 1K, as from the AC susceptibility data from $x = 0.2$ and $x = 0.3$, it seems evident that by this temperature all magnetic order has been destroyed. The base temperature reached by the sample is in the range of 180 mK, and the high field corresponds to 1T.

The first comparison to be carried out is the difference between a field of 0 and 1 T at base temperature. This is carried out first, as it is believed that by applying a 1 T field along the crystal c axis, the Ho moments should be polarised in the field direction. Figure 4.3 shows a comparison of a3 scans (which implies rotating the crystal) taken around the (200) and (004) Bragg peaks. Both these peaks correspond to ferromagnetic order, with the (200) peak corresponding to order along the c axis and (004) corresponding to order along the a axis.

Due to some mosaicity of the sample, due to slight misalignment between the individual wafers inside the sample holder, the Bragg peaks do not fit well with a single Gaussian as would be expected for long range order. In the case of short range order, the peaks should fit a Voigt curve (a convolution of a Gaussian and a Lorentzian), however this is also not

the case. To fit the curves, two Gaussians are used, implying that the sample behaves more or less like two crystals which have a slight misalignment. Using a double Gaussian fit, the change in the intensity of the peak is found to be $< 1\%$ for the (200) peak and $5.5 \pm 0.5\%$ for the (004) peak. This result is very surprising, as one would expect the Ho ions to align along the Ising axis parallel to the field. One possible reason why this does not happen is that the Er ions may not stay in the a-b plane and the Ho ions will therefore interact with the Er ions through the dipole interaction, leading to an alignment along the a axis.

These two graphs also show a problem which was encountered in running field scans on this sample. It seems that the force generated by the ferromagnetic moments in the field is enough to turn the entire dilution fridge by a few fractions of a degree. Although this does not seem like a large amount, it can have disastrous effects when a field scan is carried out while sitting on a Bragg peak. For this reason, the field scans which were done while sitting on both the (200) and (004) Bragg peaks are not examined here, as there is no guarantee that the apparent dependence is actually that of the magnetic order.

The reason why this change of the position of the sample is such a problem is that field scans seemed to indicate that the increase in magnetic order along the a axis corresponded to a drop in the peak intensity at (200), although this is almost essentially ruled out by the a3 scans already mentioned. To see if it is possible that a 1% change in signal could correspond to the creation of long range order, the expected maximum signal from order must be calculated. Previous experiments on pure $LiHoF_4$ carried out by Rønnow show that the magnetic signal from the ferromagnet is roughly the same intensity as that from the nuclear order [25]. If it is assumed that all the moments are aligned ferromagnetically, then the increase in intensity from a sample with 25% of the ions being Ho should be 6.25%. If the situation isn't as ideal and for example some of the moments are not aligned and perhaps those which are aligned have not reached the maximum expectation value, then a 1% change in signal intensity could imply a long range order.

Looking at these peaks at high and low temperature, there does not appear to be a very large difference in the signal intensity, as can be seen in Figure 4.4. Once again the fit used for the curves is two Gaussians, which in this case gives changes of $< 1\%$ for both the (200) and (004) Bragg peaks. The problem here is that the error for the points is also on the order of 1%, which means that it can't be said with any certainty if there is or isn't long range order. To be sure of this, the curves would need to be taken again with higher statistics.

4.3.2 Antiferromagnetic correlations

As was the case with the ferromagnetic correlations, the antiferromagnetic correlations are investigated by comparing scans around the (100) peak. Scans are taken along the

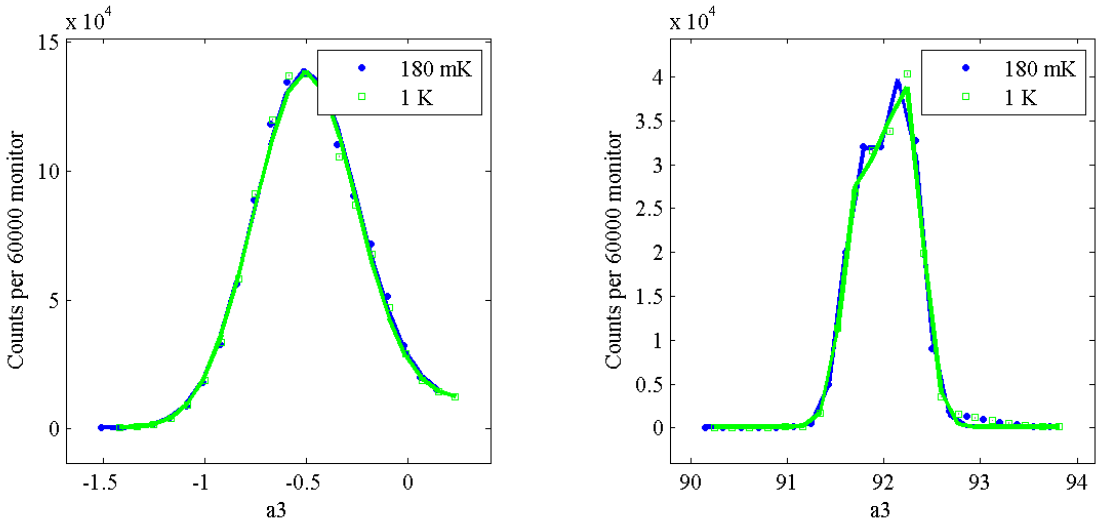

(a) (b)

Figure 4.4: Temperature dependence of the (a) (200) and (b) (004) Bragg peaks.

(1,0,l) direction at 180 mK and 1K in zero field along with 180 mK in a 1 T field. Figure 4.5 shows the data obtained at 180 mK and 1 K after having the signal at 180 mK with a field of 1 T subtracted. The 180 mK and 1 T scan is taken as a background firstly as the intensity is less than that at 1K but also because in the presence of the field, spins are less able to fluctuate.

The data shows that there are clearly short range antiferromagnetic correlations present in the system. In the case of short range correlations, the line shape should be that of a Lorentzian, however in this case the situation is slightly more complex. The fit should in fact be made of two Lorentzians, one centered at (100) and another centered at (102). The inclusion of the second peak is important as the extent of the peaks implies that there is likely an overlap between the two. Not taking this overlap into account would lead to a fit which could determine the FWHM of the peak to be larger than it actually is. The lines on the graph correspond to this double Lorentzian fit.

The difference between the two curves taken at 180 mK is due to the long thermalisation times of the sample. In the case of the blue data set, the sample had been at base temperature for a number of days before the scan was taken. The red data set was obtained straight after the sample had been cooled down from 1K. The lower intensity of the peak in this data set is therefore most likely due to the temperature being slightly warmer than for the blue data set. The extremely wide Lorentzian present in the 1 K scan implies that there is still some kind of short range correlations at this temperature. The large FWHM compared to that seen at 180 mK implies that the order is much shorter

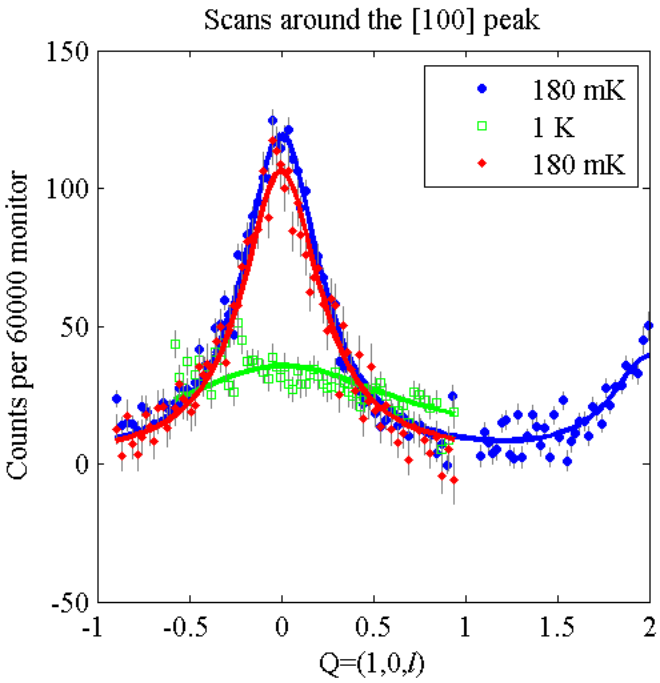

Figure 4.5: Temperature and field dependence of the (100) peak. Scans taken at 180 mK and 1 K in zero field are subtracted from a scan taken at 180 mK in a 1T field. The blue points correspond to a scan taken after the sample being cold for a long time compared to the red points, where the scan was started immediately after cooling. The lines are a fit of two Lorentzians, one peaked at (100) and the second peaked at (102).

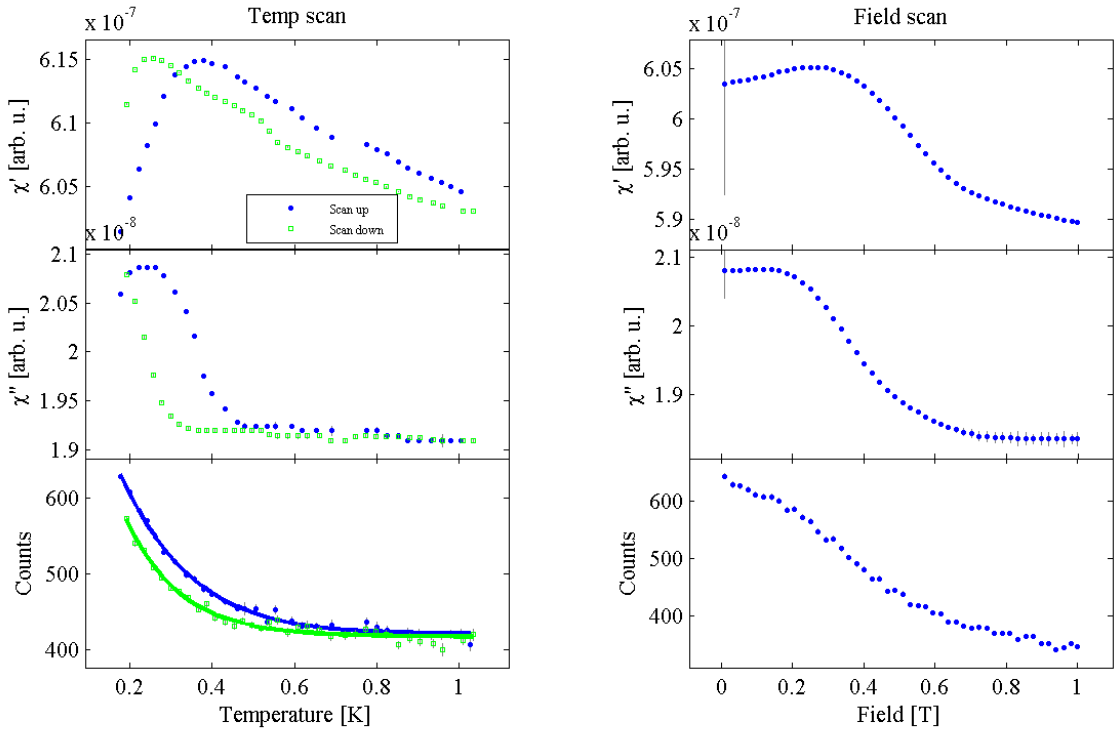

(a) (b)

Figure 4.6: (a) Temperature scan and (b) Field scan on the [100] peak. The scans combine both AC susceptibility and neutron scattering data.

ranged.

Along with the scans around the (100) peak, the temperature and field dependence of this peak is also measured. This is done by measuring (100) as the field and temperature are changed. This is a very slow procedure due to the long thermalisation times of the sample in the case of a temperature scan and the possible eddy current heating in a field scan. As the eddy current heating is proportional to the ramping rate of the DC field squared [21], the field can't be ramped at a rate faster than 0.002 T/min without heating the sample. In the case of a temperature scan, the thermalisation depends on the relative temperature of the sample - the lower the sample temperature, the worse the thermalisation. For this reason the temperature is ramped at 1 mK / min for $0 < T < 250$ mK, 2 mK / min for $250 < T < 500$ mK and 5 mK / min for $500 < T < 1000$ mK. The data obtained for both temperature and field scans is shown in Figure 4.6 (a) and (b) respectively.

This data is unique as the AC susceptibility is measured at the same time as the neutron scattering data is taken. The susceptibility data is taken using an excitation current of 100

μA at a frequency of 990 Hz. The temperature scan is taken both scanning up and down in temperature. This is useful as it gives an idea to the relative temperature difference between the sample thermometer and the sample. If both temperatures were identical at all times, the two curves in the susceptibility should overlap perfectly. As this is not the case, it is clear that the temperature of the sample lags that of the thermometer. It should however also be noted that the bulk of the sample may be better thermalised than the area being measured by the coils. This is due to the fact that the copper foils used to thermalise the sample do not extend all the way to the end of the piece whose susceptibility is measured. The result of this is that the heat has to be conducted through a distance of 5 mm in this part of the sample compared to ~ 0.7 mm in the rest. Keeping this in mind, it seems that at the ordering temperature, the difference between the sample and thermometer is at most 50 mK.

An analysis of the temperature scan shows that the features of the AC susceptibility scan are not present in the neutron scattering data. The neutron scattering data has been fit to a power law and appears to be a good fit. The difference between the susceptibility and neutron data is perhaps not so surprising when the measurements themselves are taken into account. In the AC susceptibility, the peak seen corresponds to the formation of clusters whose relaxation rate is 990 Hz. As these clusters begin to form from paramagnetic spins, χ' increases. Once these clusters have been formed and are effectively frozen into place, χ' decreases as the clusters are less and less able to respond to the field as the temperature decreases further. On the other hand, the neutron scattering gives information on the correlation length of the spins, therefore a sharp transition is not necessary.

In the case of the field scan, it does seem that the susceptibility and neutron scattering data are related. In particular there is a striking resemblance between χ' and the intensity of the (100) peak, although the features are less pronounced in the neutron scattering data.

5 Conclusion

To draw a conclusion on the work carried out for this thesis is rather difficult, as it seems that the calculations and experiments carried out barely scratch the surface of the $LiHo_xEr_{1-x}F_4$ alloy. I will therefore try to conclude about the theory, AC susceptibility and neutron scattering data separately, indicating where further work could focus.

From the AC susceptibility data, it seems that the mean field calculation using a virtual crystal approximation is inadequate to describe this system. This is made evident by the fact that the calculation always predicts some kind of long range order, where as it is seen that for $x < 0.5$ there is no long range order, but only a spin glass state. The good agreement in terms of T_c is most likely only a coincidence. The shortcomings are most likely due to the inability of the virtual crystal approximation to correctly take into account the interactions between Ho and Er ions. One possible alternative, which has been carried out on the $LiHo_xY_{1-x}F_4$ dilute Ising magnet is to use instead of a virtual crystal a real space alloy mean field calculation .

Focusing on the AC susceptibility data the system can be to some extent characterised. For large x ($x > 0.5$) the system appears to form a Ising ferromagnet at high temperatures and then clusters into what appears to be a superparamagnetic state at lower temperatures. For all lower concentrations of Ho, the system behaves somewhat like a insulating spin glass compound. It is somewhat unfortunate that there was not sufficient time to carry out more AC susceptibility measurements, as there is much more work to be done. The most interesting direction is almost certainly investigating the possibility of any quantum critical behaviour in the presence of a field. This requires the AC susceptibility of single crystals to be measured along both the a and c axes while applying a field transverse to the measurement direction. It would also be beneficial to study the frequency dependence of the frozen short range ordered states and also investigate if there is any hysteresis or memory effects commonly seen in spin glasses.

The neutron scattering data brought many interesting revelations about the kind of order being formed. The frozen clusters inside the system for $x = 0.25$ were found to be ordered antiferromagnetically. The lack of any long range order verified the results found in the AC susceptibility measurements taken for the neighbouring samples. The real surprise is that in the presence of a field parallel to the Ising axis, the Ho moments align ferromagnetically perpendicular to this axis. This is a very good indication that the Ho

and Er ions do indeed interact a lot with each other. Further work with neutron scattering should focus on better understanding of the strange field dependence seen, including the application of the field transverse to the Ising axis. It would also be interesting to see if the clusters formed are always antiferromagnetic, or if as x is increased, the clusters become ferromagnetic in nature.

Apart from getting improved measurements on the samples already available, it would be interesting to investigate regions where the physics changes. There exists somewhere between $x = 0.8$ and $x = 0.5$ a cross-over where the system changes from long range order to a glassy state and it would be interesting to see how the sample behaves around this possible quantum critical point. The same kind of investigation could take place for small x, where the system changes from a antiferromagnet to this glassy state.

Bibliography

[1] Amnon Aharony, *New singularities in the critical behavior of random ising models at marginal dimensionalities*, Phys. Rev. B **13** (1976), no. 5, 2092–2098.

[2] J E Battison, A Kasten, M J M Leask, J B Lowry, and B M Wanklyn, *Ferromagnetism in lithium holmium fluoride-lihof4. ii. optical and spectroscopic measurements*, Journal of Physics C: Solid State Physics **8** (1975), no. 23, 4089–4095.

[3] P. Beauvillain, J-P Renard, and P-E Hansen, *Low-temperature magnetic susceptibility of $LiErF_4$:evidence of antiferromagnetic ordering at 0.38k*, J.Phys.C: Solid State Phys **10** (1977), 709–712.

[4] P. Beauvillain, J-P Renard, and J. Magarino, *Determination of crystal field parameters of lirf 4 (r = tb, ho, er) by high temperature susceptibility measurements*, Journal of Magnetism and Magnetic Materials **15-18** (1980), 31–32.

[5] K BINDER and AP YOUNG, *SPIN-GLASSES - EXPERIMENTAL FACTS, THEORETICAL CONCEPTS, AND OPEN QUESTIONS*, REVIEWS OF MODERN PHYSICS **58** (1986), no. 4, 801–976 (English).

[6] D Bitko and T. F. Rosenbaum, *Quantum behavior for a model magnet*, Physical Review Letters **77** (1996), 940–943.

[7] J Brooke, *Quantum fluctuations and disorder in a model magnet*, Ph.D. thesis, University of Chicago, 2000.

[8] N. Craig and T. Lester, *Hitchhiker's guide to the dilution refrigerator*, 2004.

[9] S Ghosh, *Non-linear dynamics in spin liquids*, Ph.D. thesis, THE UNIVERSITY OF CHICAGO, 2003.

[10] P. E. Hansen, T. Johansson, and R. Nevald, *Magnetic properties of lithium rare-earth fluorides: Ferromagnetism in $lierf_4$ and $lihof_4$ and crystal-field parameters at the rare-earth and li sites*, Phys. Rev. B **12** (1975), no. 11, 5315–5324.

[11] M. T. Hutchings, *Solid state physics*, vol. 2, Academic Press, New York, 1964.

[12] Stine Nyborg Klausen, *Manual for the rita2 spectrometer, http://sinq.web.psi.ch/sinq/instr/rita2/htdocs/misc/shortusermanual.html.*, LNS, 0 ed., 2001.

[13] C Kraemer, *Magnetic properties of lierf_4.*

[14] C. Kraemer, *Magnetische eigenschaften von lierf4 - eine untersuchung mittels neutronenstreung*, Master's thesis, Laboratory for Neutron Scattering ETH Zurich & Paul Scherrer Institute CH-5232 Villigen PSI, 2006.

[15] J Magarino and J Tuchendler, *Epr experiments in litbf_4, lihof$_4$ and lierf_4 at submillimeter frequencies*, Phys. Rev. B **21** (1980), no. 1, 18–28.

[16] G. Mennenga, L. J. Jongh, and W. J. Huiskamp, *A comparative study of the magnetic ordering specific heats of four s = 1/2 dipolar magnets: Lirf_4 (r=er, dy, ho, tb)*, Journal of Magnetism and Magnetic Materials **44** (1984), 48–58.

[17] S. K. Misra and J. Felsteiner, *Low-temperature ordered states of lithium rare-earth tetrafluorides (lirf_4)*, Phys. Rev. B **15** (1977), no. 9, 4309–4312.

[18] J. A. Mydosh, *Spin glasses: An experimental introduction*, Taylor & Francis, 1993.

[19] M Nikolo, *Superconductivity: A guide to alternating current susceptibility measurements and alternating current susceptometer design*, American Journal of Physics **63** (1995), 57–65.

[20] C. Pfleiderer, *Miniature ac susceptometers for use inside clamp type pressure cells*, Review of Scientific Instruments **68** (1997), no. 3, 1532–1535.

[21] F. Pobell, *Matter and methods at low temperatures*, third ed., Springer, 2007.

[22] J. A. Quilliam, S. Meng, C. G. A. Mugford, and J. B. Kycia, *Evidence of Spin Glass Dynamics in Dilute LiHoxY1-xF4*, PHYSICAL REVIEW LETTERS **101** (2008), no. 18, 187204.

[23] J. A. Quilliam, C. G. A. Mugford, A. Gomez, S. W. Kycia, and J. B. Kycia, *Specific heat of the dilute ising magnet liho[sub x]y[sub 1-x]f[sub 4]*, Physical Review Letters **98** (2007), no. 3, 037203.

[24] D. H. Reich, T. F. Rosenbaum, G. Aeppli, and H. J. Guggenheim, *Ferromagnetism, glassiness, and metastability in a dilute dipolar-coupled magnet*, Phys. Rev. B **34** (1986), no. 7, 4956–4958.

[25] Rønnow, *D10 experimental report.*

[26] H. M. Rønnow, J. Jensen, R. Parthasarathy, G. Aeppli, T. F. Rosenbaum, D. F. McMorrow, and C. Kraemer, *Magnetic excitations near the quantum phase transition in the ising ferromagnet lihof[sub 4]*, Physical Review B (Condensed Matter and Materials Physics) **75** (2007), no. 5, 054426.

[27] G. L. Squires, *Introduction to the theory of thermal neutron scattering*, Dover Publications, 1997.

[28] K.-M. Tam and M. J. P. Gingras, *Spin Glass Transition at Nonzero Temperature in a Disordered Dipolar System: The Case of LiHoxY{1-x}F4*, ArXiv e-prints (2008).

[29] C. E. Torres, *Relaxation in quantum glasses*, Ph.D. thesis, University of Chicago, 2007.